Regulation of Ebola GP conformation and membrane binding by the chemical environment of the late endosome

Aastha Jain[1], Ramesh Govindan[1,2], Alexander Berkman[1], Jeremy Luban[3,4], Marco A. Díaz-Salinas[1], Natasha D. Durham[1], James B. Munro[1,4*]

[1]Department of Microbiology and Physiological Systems, UMass Chan Medical School, Worcester, MA, USA

[2]Medical Scientist Training Program, Tufts University School of Medicine, Boston, MA

[3]Program in Molecular Medicine, UMass Chan Medical School, Worcester, MA

[4]Department of Biochemistry and Molecular Biotechnology, UMass Chan Medical School, Worcester, MA

*Correspondence: james.munro@umassmed.edu

Abstract

Interaction between the Ebola virus envelope glycoprotein (GP) and the endosomal membrane is an essential step during virus entry into the cell. Acidic pH and Ca^{2+} have been implicated in mediating the GP-membrane interaction. However, the molecular mechanism by which these environmental factors regulate the conformational changes that enable engagement of GP with the target membrane is unknown. Here, we apply fluorescence correlation spectroscopy (FCS) and single-molecule Förster resonance energy transfer (smFRET) imaging to elucidate how the acidic pH, Ca^{2+} and anionic phospholipids in the late endosome promote GP-membrane interaction, thereby facilitating virus entry. We find that bis(monoacylglycero)phosphate (BMP), which is specific to the late endosome, is especially critical in determining the Ca^{2+}-dependence of the GP-membrane interaction. Molecular dynamics (MD) simulations suggested residues in GP that sense pH and induce conformational changes that make the fusion loop available for insertion into the membrane. We similarly confirm residues in the fusion loop that mediate GP's interaction with Ca^{2+}, which likely promotes local conformational changes in the fusion loop and mediates electrostatic interactions with the anionic phospholipids. Collectively, our results provide a mechanistic understanding of how the environment of the late endosome regulates the timing and efficiency of virus entry.

Author Summary

Ebola virus causes disease in humans with high fatality. A better understanding of how Ebola virus enters cells is critical to inform the development of novel therapeutic and preventative measures. The viral glycoprotein present on the surface of the virus mediates attachment to cells and subsequent entry through a poorly understood mechanism involving fusion of viral and cellular membranes. Here, we employ computational and experimental biophysical techniques to understand how the Ebola glycoprotein senses chemical cues in its environment, such as pH, calcium ions, and specific lipid species to ensure that entry occurs at the right time and place. Our results specify elements of the glycoprotein that control its structure under changing physiological environments.

42 **Introduction**

43 Ebola virus (EBOV) causes disease in humans with an average case fatality rate of 50% [1]. Incidences of
44 repetitive outbreaks, changes in virulence, or emergence of resistance could reduce the effectiveness of
45 currently approved vaccination and treatment regimes. Therefore, a better understanding of the EBOV
46 entry mechanism, an under-utilized drug target, would aid in the development of effective prophylactic
47 and treatment interventions. The EBOV envelope glycoprotein (GP), present on the surface of the virion,
48 mediates virus entry into host cells. GP is a trimer of heterodimers with each protomer consisting of two
49 subunits, GP1 and GP2, which are linked by disulfide bonds [2]. Virions attach to the host cell surface via
50 GP1 interaction with C-type lectins and phosphatidylserine receptors, and are internalized by
51 macropinocytosis [3,4]. Once inside the endosomes, cathepsins B and L proteolytically remove the mucin-
52 like domain and glycan cap from GP1, enabling its binding to the endosomal receptor, the Niemann-Pick
53 C1 (NPC1) cholesterol transporter [5–8]. Conformational changes in GP, which occur in response to cues
54 encountered in the endosome, reposition the fusion loop of GP2 from a hydrophobic cleft in the
55 neighboring protomer to a position where it can insert into the endosomal membrane. Additional factors
56 yet to be identified are likely required to trigger the complete cascade of conformational changes in GP
57 needed to promote fusion of the viral and endosomal membranes [9].

58 While in the endocytic pathway, acidification of the endosomal lumen and Ca^{2+} play critical, but poorly
59 defined roles in promoting EBOV entry [10–14]. Our previous single-molecule Förster resonance energy
60 transfer (smFRET) experiments using intact, trimeric GP on the surface of pseudoviral particles
61 demonstrated that low pH and Ca^{2+} promote conformational changes in GP that correlate with lipid mixing
62 [12]. A recent study further showed that in addition to low pH and Ca^{2+}, cathepsins enhanced the fusion
63 of GP-containing pseudoparticles with supported phospholipid bilayers formed from endosomal
64 membranes [15]. In a prior study of a GP fragment (residues 507-560) containing the fusion loop,

65 conserved residues were mutated to identify pH sensors that control membrane binding and fusion [16].
66 Only mutation of H516 reduced lipid mixing by 80% in an *in vitro* assay. However, no single amino acid
67 within the fusion loop could be conclusively identified as a pH sensor that could trigger efficient lipid
68 mixing or cell entry. Another study investigated the interaction of Ca^{2+} ions with anionic residues flanking
69 the fusion loop [14]. Residues D522 and E540 were crucial for interaction with Ca^{2+} of a GP fragment
70 containing the fusion loop, which enhanced membrane binding. While these studies suggested residues
71 in the fusion loop that are involved in sensing pH and Ca^{2+}, the role of these residues in mediating
72 conformational changes of trimeric GP has not been evaluated. Nor has it been determined how
73 additional residues outside of the fusion loop might allosterically regulate conformational dynamics of GP
74 and fusion loop-mediated membrane binding.

75 Lipids in host cell membranes can facilitate virus attachment and regulate fusion. The lipid content of
76 endosomes is important in sorting of enveloped viruses into specific compartments and avoiding
77 premature fusion [17]. The late endosomal membrane is rich in the anionic lipids phosphatidylserine (PS)
78 and bis(monoacylglycero)phosphate (BMP) [18,19]. BMP is essential for fusion of viruses such as Dengue,
79 Lassa, Uukuniemei and vesicular stomatitis virus that enter cells through the endocytic route [20–24].
80 However, a role for BMP in EBOV GP entry could not be verified using a cell-cell fusion assay [9]. This may
81 indicate that the plasma membrane lacks other lipid or protein components, which are specific to the
82 endosome and essential for EBOV GP-mediated fusion. Therefore, whether endosomal lipids play a role
83 in EBOV entry remains an open question.

84 In the present study, we sought to elucidate the mechanistic basis for how the chemical features of the
85 late endosome enable GP to engage the target membrane prior to fusion. To probe the ability of trimeric
86 GP to bind membranes of defined composition, we developed a fluorescence correlation spectroscopy
87 (FCS) assay. FCS provides quantitative information on the diffusion of molecules in solution. In comparison

88 to conventional pull-down or membrane flotation methods, FCS has high spatio-temporal resolution,
89 requires low sample quantity, and provides rapid experimental throughput [25]. Our results indicate that
90 the anionic lipids PS and BMP enhance the GP-membrane interaction. Furthermore, we demonstrate that
91 BMP is the primary mediator of Ca^{2+}-dependence for this interaction. Parallel smFRET imaging indicated
92 that acidic pH is the primary driver of global GP conformational changes, which move the fusion loop away
93 from its hydrophobic cleft to a position where it can engage the membrane. Ca^{2+} binding to the fusion
94 loop may have a more localized effect on GP conformation. The results of mutagenesis support a model
95 in which pH- and Ca^{2+}-sensing residues tune the responsiveness of GP to the chemical environment of the
96 late endosome, ensuring proper timing of conformational changes necessary for fusion.

97 **Results**

98 ***Anionic lipids and Ca^{2+} mediate GP-membrane binding at acidic pH***

99 We first developed an *in-vitro* FCS assay to quantify the interaction between GP and model membranes
100 (**Figure 1A**). The trimeric ectodomain of GP (GPΔTM) from the Mayinga strain of EBOV, lacking the
101 transmembrane and mucin-like domains, was expressed and purified in Expi293 cells. GPΔTM was site-
102 specifically labelled with Cy5 using an enzymatic labelling approach (Materials and Methods) [26]. After
103 proteolytic removal of the glycan cap with HRV3C from labelled GPΔTM (forming GP^{CL}), FCS measurements
104 showed that GP^{CL} diffused as a single homogeneous species with a diffusion time of 0.308 ± 0.007 ms
105 (**Figure 1B**). We then prepared 100-nm liposomes using phosphatidylcholine (PC), cholesterol (Ch), and
106 the lipophilic fluorophore DiD (PC:Ch:DiD 95:5:0.04mol%). FCS indicated a diffusion time of 2.6 ± 0.2 ms
107 for the liposomes, reflecting their larger size and slower motility than GP^{CL} (**Figure 1C**). To facilitate GP^{CL}-
108 membrane interactions under conditions that approximate the late endosome, we incubated GP^{CL} with
109 unlabeled liposomes (PC:Ch 95:5mol%) at 37°C for 20 mins at pH 5.5. Evaluation with FCS indicated a
110 mixture of two species with diffusion times consistent with unbound GP^{CL} (*ca.* 0.3 ms), and GP^{CL} bound to

111 liposomes (*ca.* 2.6 ms). Under these conditions, 4.8 ± 0.1% of GP^{CL} bound to the zwitterionic liposomes
112 (**Figure 1D**). Introduction of Ca^{2+} at concentrations as high as 1 mM had minimal effect.

113 We then sought to optimize the lipid composition such that we could robustly detect GP^{CL} binding to
114 liposomes and later evaluate the role of specific GP^{CL} residues and Ca^{2+}. We specifically asked whether
115 inclusion of anionic phospholipids found in the late endosome, such as PS and BMP, might further
116 promote GP^{CL}-membrane interaction. Introduction of PS into the liposomes (PC:PS:Ch 55:40:5mol%)
117 increased GP^{CL} binding to 10.9 ± 0.2% in the absence of Ca^{2+}. Addition of Ca^{2+} at concentrations of 1 μM
118 and 10 μM further increased GP^{CL} binding to 17.9 ± 0.3% and 27.5 ± 0.2%, respectively (**Figure 1D**). Further
119 increases in Ca^{2+} concentration reduced GP^{CL} binding. Inclusion of BMP (PC:PS:BMP:Ch 40:40:15:5mol%),
120 an anionic lipid specific to late endosomes [19,27], further increased GP^{CL}-membrane interaction to 26.7
121 ± 0.2% in the absence of Ca^{2+}. Stepwise increase in Ca^{2+} to 1 mM led to 52.0 ± 0.3% bound GP^{CL} (**Figure**
122 **1D**). However, the Ca^{2+}-dependence of GP^{CL} binding to the PC:PS:BMP:Ch membrane was only apparent
123 at acidic pH; Ca^{2+} did not promote GP^{CL}-membrane interaction at neutral pH (**Figure 1E**). These data
124 demonstrate that the anionic phospholipids PS and BMP promote GP^{CL} binding to model membranes in a
125 pH- and Ca^{2+}-dependent manner.

126 Based on these results, we next hypothesized that BMP might be the primary driver of the Ca^{2+}-
127 dependence of GP^{CL} binding to the membrane. We therefore probed the relative contributions of PS and
128 BMP to the observed GP^{CL}-membrane interaction. We titrated PS from 0 to 40mol%, while keeping the
129 BMP and Ch concentrations constant, and assessed GP^{CL} binding to liposomes in the absence and presence
130 of 1 mM Ca^{2+}. Liposomes without PS bound low levels of GP^{CL} irrespective of the presence of Ca^{2+} (**Figure**
131 **1F**). Stepwise increases in PS concentration resulted in concomitant increases in GP^{CL} binding to
132 liposomes, always with greater binding in the presence of Ca^{2+}. Calculation of the ratio of bound GP^{CL} in
133 the presence of Ca^{2+} to that seen in the absence of Ca^{2+} across the PS titration indicated a linear trend

134 with a slope not significantly different from zero (p = 0.12; **Figure 1G**). These data demonstrate that PS
135 promotes GP^{CL}-membrane binding, and thus enhances the robustness of our *in-vitro* measurements. But
136 PS is not responsible for the Ca^{2+} dependence. Instead, BMP is the more critical determinant of the Ca^{2+}-
137 dependence of GP^{CL}-membrane interaction.

138 ***Conformational dynamics of GP^{CL} during membrane binding***

139 We next sought to characterize the conformational changes of GP^{CL} that enable interaction with the
140 membrane under the conditions identified in our FCS assay. To this end, we used a previously established
141 smFRET imaging assay that reports on conformational changes in GP2 (**Figure 2A, B**) [28]. We used
142 lentiviral pseudoparticles with GP containing a non-natural amino acid, *trans*-cyclooct-2-ene-L-lysine
143 (TCO*) at positions 501 and 610, which enabled labeling with Cy3- and Cy5-tetrazine [29]. We first
144 assessed the conformational equilibrium of GP^{CL} at pH 7.5 in the absence of Ca^{2+}. Advancements in single-
145 molecule detection allowed us to resolve additional FRET states beyond what had previously been
146 reported and improved our resolution in the estimation of state occupancies (Materials and Methods)
147 [28]. Hidden Markov modelling (HMM) of the individual smFRET traces indicated the existence of four
148 conformational states with FRET efficiencies of 0.24 ± 0.08, 0.49 ± 0.08, 0.72 ± 0.08, and 0.92 ± 0.08 (**Figure**
149 **2C**). The 0.92-FRET state (high FRET), which is consistent with the pre-fusion conformation reflected in
150 structures of GP [2,30,31], predominated with 35 ± 2% occupancy (**Figure 2D, E**). HMM analysis indicated
151 spontaneous transitions among the four FRET states and enabled construction of a transition density plot
152 (TDP), which displays the relative frequency of transitions (**Figure 2F**). The TDP indicates that most
153 transitions occur into and out of the 0.92-FRET state (high FRET), and between the 0.72- and 0.49-FRET
154 states. Transitions into and out of the 0.24-FRET state (low FRET) were comparatively rare.

155 Given the sites of fluorophore attachment, we hypothesized that the low-FRET state might reflect a
156 conformation in which the fusion loop was released from the hydrophobic cleft to positions where it can

157 engage the target membrane. The 0.72- and 0.49-FRET states may reflect intermediate conformations
158 where the fusion loop is destabilized prior to release from the hydrophobic cleft. Acidification to pH 5.5
159 reduced the occupancy of the high-FRET pre-fusion conformation to 14 ± 2% (**Figure 2D, E**). The
160 occupancies in the 0.49- and low-FRET states increased and more frequent transitions occurred into and
161 out of the low-FRET state. The addition of 1 mM Ca^{2+} increased the kinetics of transitions into and out of
162 the low-FRET state, while minimally affecting the thermodynamics of the FRET distribution (**Figure 2D-F**).

163 Next, we incubated the labelled pseudovirions with PC:PS:BMP:Ch liposomes at pH 5.5 in the presence of
164 1 mM Ca^{2+}. Our FCS experiments had indicated robust membrane binding under these conditions.
165 Interaction with liposomes decreased the occupancy in the high-FRET pre-fusion conformation, as well as
166 the 0.72- and 0.49-FRET states, while increasing the low-FRET state occupancy to 54 ± 2% (**Figure 2D, E**).
167 Overall dynamics of GP^{CL} also decreased significantly with remaining transitions occurring in and out of
168 the low-FRET state (**Figure 2F**). Taken together, these data identify the low-FRET state as a GP^{CL}
169 conformation that is enriched at pH 5.5 and stabilized by interaction with a target membrane, suggesting
170 the release of the fusion loop from the hydrophobic cleft.

171 ***MD simulations predict GP residues involved in sensing changes in pH***

172 We next used molecular modelling to predict residues in the trimeric GP^{CL} ectodomain that sense changes
173 in pH and control the conformational transitions necessary for membrane binding. We ran constant-pH
174 molecular dynamics (MD) simulations using atomic coordinates of the trimeric GP^{CL} ectodomain [31,32].
175 These simulations enabled estimation of the fractional protonation state of each protonatable residue in
176 GP^{CL} at pH values ranging from 4.2 to 7.5. The resulting simulated titrations were fit to the Hill equation
177 to determine estimates of the pK_As and Hill coefficients for each residue. Simulations of trimeric GP^{CL} were
178 run in triplicate, providing a total of 9 sets of pK_As and Hill coefficients. Not surprisingly, our simulations
179 indicated that the five histidines in the GP^{CL} ectodomain—H39, H139, H154, H516, and H549—had pK_A

180 values of 6.78, 5.04, 5.50, 6.44, and 6.17, respectively (**Figure 3**). These data suggest that these five
181 histidines become protonated, likely at different times, during trafficking of EBOV through the endocytic
182 pathway.

183 We next used equilibrium MD simulations to generate specific hypotheses about how the histidines
184 contribute to mediating pH-induced GP^{CL} conformational changes. Following minimization and a multi-
185 step equilibration procedure (Materials and Methods), simulations of GP^{CL} were run in triplicate for 250
186 ns. Thus, we obtained 750 ns of aggregate sampling for each of the three protomers in the GP^{CL} trimer
187 with either deprotonated or protonated histidines. The simulation of protonated histidines was meant to
188 approximate the conditions of the acidic late endosome. We first calculated the root-mean-square-
189 fluctuation (RMSF) for each residue in GP^{CL}, which quantifies the amplitude of dynamics. We then
190 averaged the RMSFs across the three protomers and the three replicas for the unprotonated and
191 protonated simulations. The difference in average RMSF for the two simulations reports on whether each
192 residue was more dynamic in the unprotonated or protonated simulation. The fusion loop residues D522
193 through E540, which includes the hydrophobic patch shown to interact directly with the membrane
194 [33,34], displayed greater dynamics in the protonated simulation, suggesting destabilization of the fusion
195 loop in the hydrophobic cleft (**Figure 4A-C**). Residue Y534 is notable due to its proximity to H154 of the
196 neighbouring protomer. The simulations predict an electrostatic interaction between the backbones of
197 Y534 and H154, which may stabilize the fusion loop in the hydrophobic cleft. At the same time, the H154
198 side chain is engaged in electrostatics with the E178 side chain. Fluctuations in the H154-E178 distance
199 decrease after protonation of H154, suggesting stabilization of the H154-E178 interaction. Additionally,
200 the distance between H154 and Y534 increased upon protonation of H154 from approximately 3.4 to 4.6
201 Å (**Figure 4D-F**). This analysis suggests the hypothesis that protonation of H154 in GP1 aids in release of
202 the GP2 fusion loop of the neighbouring protomer by weakening the interaction with Y534.

203 We also noted that H516, which flanks the hydrophobic patch in the fusion loop, is engaged in a Pi-Pi
204 stacking interaction with the side chain of W104 in GP1. The simulation suggests that this interaction is
205 labile when H516 is deprotonated, with H516 sampling multiple conformations (**Figure 4G, H**). These
206 dynamics can be visualized in terms of the distance between H516 and W104, and the χ_2 dihedral angle
207 of the H516 side chain. Protonation of H516 stabilized the stacking interaction with W104, reducing the
208 dynamics of H516 and selecting a single pre-existing conformation (**Figure 4G-I**). These data suggest that
209 GP1-GP2 interaction may be critical to GP2 conformational changes that remove the fusion loop from the
210 hydrophobic cleft and stabilize it in a position competent for engagement with the membrane. While the
211 remaining histidines—H39, H139, and H549—likely undergo changes in their protonation state during
212 virus internalization and trafficking, our MD simulations do not indicate that protonation alters their
213 dynamics or local interactions. We therefore consider it unlikely that these residues play a central role in
214 mediating pH-dependent conformational changes in trimeric GP^{CL}. Going forward, we focused our
215 attention on H154 and H516 and the predictions made by our simulations.

216 ***H154 in GP1 mediates GP2 conformation at acidic pH***

217 We next used our FCS and smFRET assays to test the predictions of our MD simulations regarding the role
218 of H154 in mediating the conformational changes in trimeric GP^{CL} that enable membrane binding. First,
219 we introduced an alanine substitution at residue H154, which eliminates the putative interaction with
220 E178. Consistent with a previous study [35], full-length GP lacking the mucin domain (GPΔmuc) with the
221 H154A mutation expressed at a lower level than wild-type GPΔmuc, resulting in reduced—though readily
222 detectable—incorporation into pseudovirions (**Figure S2**). Also consistently, the H154A mutant showed
223 undetectable infectivity. Previous work also implicated H154A in poor proteolytic processing by cathepsin
224 L [36]. Our use of the HRV3C protease likely alleviated this limitation. When the mutation was introduced
225 in the context of our soluble GPΔTM ectodomain the native tertiary structure was verified by ELISA using

226 KZ52, an antibody specific to the native tertiary structure of GP^{CL} (**Figure S3**) [2,37]. In our FCS assay, the
227 H154A mutant bound PC:PS:BMP:Ch liposomes at a low level at pH 7.5, similarly to wild-type GP^{CL},
228 irrespective of the presence of Ca^{2+} (**Figure 5A**). smFRET imaging revealed a conformational landscape
229 that included the same four FRET states as observed for wild-type GP^{CL}, further evidence that the mutation
230 did not induce a folding defect (**Figure 5B**). However, the relative occupancies of the four FRET states were
231 distinct from wild-type and dynamics were increased overall. The occupancy of the pre-fusion
232 conformation was reduced from 35 ± 2% for wild-type to 25 ± 3% for H154A, while the occupancy in the
233 0.49-FRET state increased from 19 ± 2% for wild-type to 30 ± 2% for H154A (**Figure 5B, G**). Reducing the
234 pH to 5.5 failed to promote any further membrane binding, again regardless of the presence of Ca^{2+}
235 (**Figure 5A**). While a slight increase in transitions to the low-FRET state was seen in the TDP, no effect on
236 the FRET distribution could be detected (**Figure 5B, G, I**). These data suggest that the H154A mutation
237 destabilizes the pre-fusion conformation but prevents pH-induced stabilization of the low-FRET state,
238 consistent with its lack of binding to liposomes.

239 To further test the importance of the electrostatic interaction between H154 and E178, we introduced
240 the positively charged H154K mutation. We hypothesized that the electrostatic interaction between
241 H154K and E178 would stabilize the low-FRET conformation without dependence on pH. We observed
242 only minimal interaction of the H154K mutant with the membrane at neutral pH. Addition of Ca^{2+} induced
243 a small, but statistically significant, increase in membrane binding. At acidic pH, we observed an increase
244 in membrane binding, which was further enhanced by the presence of Ca^{2+} (**Figure 5C**). Again, our smFRET
245 data indicated the same four FRET states as seen for wild-type GP^{CL}, confirming no loss of native folding.
246 But the occupancy in the high-FRET pre-fusion conformation was approximately 50% lower than wild-type
247 at neutral pH, and the low-FRET occupancy was approximately 300% greater than wild-type (**Figure 5D,**
248 **G, H**). This significant shift in the conformational equilibrium is also reflected by the loss of recognition by
249 KZ52. Given the location of the KZ52 epitope, this is consistent with displacement of the fusion loop and

250 the HR1 helix [38]. Reduction in pH had minimal effect on the conformation of the H154K mutant, with
251 only a slight increase in transitions to low FRET (**Figure 5J**). These data suggest that the presence of a
252 positive charge at position 154 is a key determinant of the stable formation of the low-FRET state.
253 However, this shift in conformational equilibrium toward low FRET was not sufficient to enable membrane
254 binding at neutral pH, suggesting that protonation of additional residues is still critical.

255 To further validate the interactions between H154, E178, and Y534 in controlling GP^{CL} conformation, we
256 introduced the E178D mutation. We hypothesized that the shorter side chain of the aspartate amino acid
257 would draw H154 away from Y534 and reduce the stability of the fusion loop. FCS experiments
258 demonstrated similar enhancement of membrane binding by acidic pH and Ca^{2+} as seen for wild-type
259 (**Figure 5E**). As expected, smFRET data showed reduced occupancy in the high-FRET pre-fusion
260 conformation, at neutral pH as compared to wild-type. Moreover, reduction in pH increased occupancy
261 in the low-FRET state to an extent greater than seen for wild-type (**Figure 5F, G**). Reduced transitions into
262 high FRET further demonstrated the relative instability of the pre-fusion conformation (**Figure 5K**).
263 Consistent with our prediction, these results suggest that upon protonation of H154, its interaction with
264 E178D strengthens, which pulls H154 away from Y534 to an extent greater than wild-type. This may lead
265 to premature release of the fusion loop at acidic pH, which could be reflected by low infectivity (**Figure**
266 **S2C**). Taken together, these results support the hypothesis suggested by our MD simulations that H154 is
267 a pH sensor that contributes to the regulation of GP conformational changes through its interactions with
268 E178 and Y534.

269 ***Protonation of H516 in GP2 further controls GP conformation***

270 We next tested the role of H516-W104 interaction in mediating GP^{CL} conformation and membrane
271 binding. The H516A mutation, which should weaken the interaction with W104, showed only low levels
272 of membrane binding in our FCS assay, with only a slight but statistically significant increase upon

273 acidification (p = 0.03), and no Ca^{2+} dependence (**Figure 6A**). In contrast, our smFRET data demonstrated
274 no significant difference in the occupancies of the high-FRET pre-fusion conformation or the low-FRET
275 state as compared to wild-type at either of the pHs tested (**Figure 6B, I**). This suggests that the H516A-
276 W104 interaction is sufficient to stabilize the low-FRET conformation, but insufficient to support
277 membrane binding. In contrast, the H516R mutation, which introduces a constitutive positive charge at
278 position 516 that enables electrostatic interaction with W104, showed robust pH-mediated membrane
279 binding, comparable to wild-type (p > 0.05; **Figure 6C**). Similarly, the H516W mutation, which can form a
280 hydrophobic stacking interaction with W104, also demonstrated enhancement of membrane binding at
281 pH 5.5 (**Figure 6E**). None of the H516 mutations demonstrated Ca^{2+} dependence during membrane
282 binding. In our smFRET experiments, at neutral pH both H516R and H516W showed reduced occupancy
283 in the high-FRET pre-fusion conformation, and increased occupancy in the low-FRET state, as compared
284 to wild-type. This is consistent with the interaction between residues 516 and 104 contributing to GP
285 conformational changes without dependence on acidic pH. For both H516R and H516W mutants,
286 acidification promoted the low-FRET state to an extent greater than for wild-type (**Figure 6D, F, I, J**),
287 perhaps indicating the combined effect of protonation of H154 and stabilization of the interaction
288 between residues 516 and 104.

289 To further interrogate the H516-W104 interaction, we introduced the W104E mutation, which we
290 predicted would support an electrostatic interaction with H516 and would be stabilized at acidic pH. The
291 W104E mutant showed only a slight, but statistically significant (p = 0.037), enhancement in membrane
292 binding at pH 5.5, which may indicate suboptimal positioning of the fusion loop (**Figure 6G**). Consistent
293 with our prediction, the W104E mutation showed greater occupancy in low FRET than wild-type at both
294 pHs tested, with the anticipated increase at pH 5.5 (**Figure 6H, J**). Taken together, these data support the
295 hypothesis that an interaction between H516 and W104 is critical for pH-mediated GP^{CL} conformational
296 changes. Stabilization of this interaction can contribute to efficiently forming the conformation reflected

297 by the low-FRET state. Mutations to H516 and W104 led to reduction in infectivity, likely indicating that
298 subsequent conformational changes necessary for fusion are inhibited (**Figure S2C**). Finally, these data
299 suggest that formation of the low-FRET conformation is not sufficient to support membrane binding, as
300 evidenced by the conformational equilibrium of H516A being indistinguishable from wild-type. This
301 implicates the local conformation of the fusion loop, which is not visualized in the current assays, in also
302 contributing to mediating interaction with phospholipids. A non-native fusion loop conformation may
303 explain the lack of Ca^{2+} dependence seen for the H516 mutants.

304 ***Acidic residues in the fusion loop are critical to GP^{CL} interaction with the membrane***

305 In the data presented above, mutations to residue H516 resulted in Ca^{2+} no longer promoting interaction
306 with the membrane even though the low-FRET state was stabilized under acidic conditions. These results
307 suggest that Ca^{2+} does not influence the global conformation of GP but rather may have a localized effect
308 on the conformation of GP2 or the fusion loop. Indeed, Ca^{2+} had minimal effect on the conformation of
309 wild-type GP^{CL} at pH 5.5 as determined by our smFRET assay (**Figure 2D, E**). Previous work identified
310 conserved acidic residues (D522, E523, E540 and E545) that mediated interaction of the fusion loop with
311 Ca^{2+} [14]. We therefore sought to test the role of these residues in the context of trimeric GP^{CL} through
312 introduction of alanine substitutions. As above, native GP^{CL} tertiary structure was evaluated using KZ52
313 ELISA (**Figure S3**). E523A and E545A were unstable in solution and were not considered further.

314 The D522A mutant bound to liposomes to a comparable extent as wild-type GP^{CL} at neutral pH (**Figure**
315 **7A**). smFRET analysis indicated a lower occupancy in the high-FRET pre-fusion conformation as compared
316 to wild-type (**Figure 7B, E**). Slightly increased dynamics as compared to wild-type were apparent in the
317 TDP, suggesting that the mutation destabilizes GP2 overall (**Figure 7G**). While membrane binding was
318 increased slightly at pH 5.5, it failed to reach the level of wild-type (**Figure 7A**). The conformational
319 equilibrium and dynamics were similar to wild-type at acidic pH, suggesting that the D522A mutation had

320 no effect on the sensitivity to pH (**Figure 7B, E**). As expected, the addition of Ca^{2+} had no effect on
321 membrane binding, conformation, or dynamics of D522A. The E540A mutation performed similarly to
322 wild-type and D522A in membrane binding at pH 7.5. However, in contrast to D522A, E540A showed
323 robust membrane binding comparable to wild-type at pH 5.5. Interestingly, Ca^{2+} inhibited E540A
324 membrane binding at pH 5.5 (**Figure 7C**). This suggests that E540A interacts with Ca^{2+} but fails to adopt a
325 fusion loop conformation that is competent for membrane insertion. Our smFRET data indicated a
326 conformational equilibrium like D522A, in which the high-FRET pre-fusion conformation was destabilized
327 as compared to wild-type at pH 7.5, but no differences in FRET state occupancies were detected at acidic
328 pH irrespective of Ca^{2+} (**Figure 7D-H**). These results indicate that the putative Ca^{2+}-binding site mediates
329 the stability of the pre-fusion GP^{CL} conformation at neutral pH but does not contribute to GP^{CL}
330 conformational changes upon acidification. The observation that the stability of the low-FRET state for
331 the D522A and E540A mutants is comparable at pH 5.5, while their membrane-binding capacities diverge
332 is further indication that transition to the low-FRET state is insufficient to support membrane binding. The
333 importance of Ca^{2+} coordination likely comes after the low-FRET conformation is achieved and prior to
334 interaction with the target membrane.

335 **Discussion**

336 Here, we report that EBOV senses chemical cues in the late endosome that promote GP^{CL} conformational
337 changes needed to initiate membrane fusion. We find that anionic lipids that are enriched in the late
338 endosome facilitate GP^{CL}-membrane binding, with BMP being especially important in mediating the Ca^{2+}-
339 dependence. We used smFRET imaging to visualize the pH-induced conformational changes in the GP2
340 subunit that enable interaction with the membrane. Molecular simulations informed hypotheses, which
341 were confirmed experimentally, suggested that H154 in GP1 and H516 in GP2 respond to changes in pH
342 and promote conformational changes in the GP^{CL} trimer. Given the differences in estimated pKas,

343 protonation of H154 and H516 may occur in series and control the stepwise promotion of conformational
344 changes. A precise structural description of the low-FRET conformation is not available. Yet, our results
345 indicate that the extent of GP^{CL}-membrane binding is inversely correlated (Pearson correlation r = -0.54,
346 p = 0.025) with the occupancy of GP^{CL} in the pre-fusion conformation (**Figure 8**), which underscores the
347 relevance of the observed conformational changes to the fusion reaction.

348 We found that GP^{CL} -membrane interaction was promoted by PS and BMP. The unique structure of BMP
349 alters the negative spontaneous curvature of membranes [39]. Additionally, BMP increases the net
350 surface charge of liposomes, enhancing their interaction with Ca^{2+} [40]. Both features of BMP may
351 promote efficient interaction between GP^{CL} and the target membrane. We speculate that GP^{CL} could
352 preferentially interact with BMP via Ca^{2+} coordination within the fusion loop. Since BMP is exclusively
353 present in the late endosome [40], it could also regulate the timing of fusion of EBOV by avoiding pre-
354 mature engagement of the fusion loop with a membrane. Dependence on BMP in regulating the location
355 and timing of fusion has been reported for other enveloped viruses such as Dengue virus, Lassa virus,
356 vesicular stomatitis virus, and influenza virus [20,21,23,41]. Whether downstream events during EBOV
357 fusion are also accelerated by BMP, as reported for Lassa virus, will be the topic of future studies [21]. PS
358 is also known to interact with Ca^{2+}, which can lead to changes in membrane curvature [42]. This altered
359 curvature could create a membrane that is not conducive to GP^{CL} binding, which may explain the reduction
360 in GP^{CL} interaction with PC:PS:Ch liposomes at elevated Ca^{2+} concentrations (**Figure 4A**) [43,44]. We
361 utilized an elevated PS concentration to optimize the extent of GP^{CL}-membrane interaction *in vitro* and
362 increase the dynamic range of our measurements. Additional components of the endosomal membrane,
363 which are yet to be identified, might further promote interaction with GP^{CL} such that elevated PS would
364 not be necessary. Nonetheless, our data indicate that the elevated PS does not impact the pH- or Ca^{2+}-
365 dependence of the GP^{CL}-membrane interaction.

366 A previous study evaluated the role of BMP during GP-mediated cell-cell fusion, concluding that BMP had
367 no effect [9]. The authors sought to incorporate BMP into the plasma membrane in the presence of
368 delipidated BSA. This approach does not enable precise control over the molar percentage of BMP, in part
369 because delipidated BSA can transport lipid moieties into the cell lumen, which may limit incorporation
370 into the plasma membrane [45,46]. Additionally, the overall lipid environment of the plasma membrane
371 is distinct from the endosome. Lipids such as PS, which our experiments suggest promotes the GP-
372 membrane interaction, and PE are enriched in the inner leaflet of the plasma membrane. In contrast, they
373 are distributed in both inner and outer leaflets in endosomes [19,47]. Hence, in a cell-cell fusion assay,
374 any role played by such lipids in GP-mediated fusion could be obscured. Our FCS-based assay enabled
375 precise control over the concentration of the lipids employed. Nonetheless, while our experiments
376 indicate that BMP promotes GP-membrane interactions, subsequent steps in the fusion reaction may
377 require unidentified factors that are not present in the plasma membrane, which might have masked the
378 effect of BMP in previous cell-cell fusion assays.

379 Protonation of histidine residues triggers membrane binding and fusion of influenza virus, Semiliki Forest
380 virus, and human metapneumoviruses [48,49]. Here, we report that residues H154 and H516 tune the
381 responsiveness of EBOV GP^{CL} to acidic pH through both stabilizing and destabilizing mechanisms. Histidine
382 residues can interact electrostatically with cationic amino acids such as lysines or arginines, forming His-
383 Cat pairs, which are known to stabilize the pre-fusion conformations of several viral envelope
384 glycoproteins [49]. Protonation of histidines destabilizes the His-Cat interaction, which contributes to
385 triggering conformational changes necessary for viral fusion. In contrast, H154 and H516 are engaged in
386 interactions not described by the His-Cat paradigm. We show here that protonation of H154 stabilizes its
387 interaction with the E178 side chain, which pulls H154 away from Y534 in the fusion loop of the
388 neighboring protomer. Destabilization of the backbone electrostatics between H154 and Y534 contributes

389 to the release of the fusion loop from the hydrophobic cleft, which facilitates the fusion loop-membrane
390 interaction.

391 A previous study concluded that H516 had no direct role in the fusion loop-membrane interaction and
392 that a positive charge at this position was insufficient to induce fusion loop-mediated membrane fusion
393 [33]. Consistent with this study, we observed similar membrane binding for the H516R mutant as for wild-
394 type GP, but with approximately 50% loss of infectivity. In this way, our results support the previous study
395 that protonation of H516 alone is not sufficient to promote robust fusion. Instead, our results suggest that
396 H516 mediates trimeric GP^{CL} conformation under acidic conditions. The apparent inter-domain Pi-Pi
397 stacking interaction between H516 and W104, which is stabilized by protonation of H516, may aid in
398 ensuring proper positioning of the fusion loop for initial interaction with the membrane. Formation of an
399 electrostatic or hydrophobic interaction of W104 with the H516R and H516W mutants, respectively,
400 supported adoption of the low-FRET conformation and membrane binding. Thus, we propose that
401 protonation of H516 aids in making the fusion loop accessible to the membrane in the context of trimeric
402 GP^{CL}. The putative H516-W104 interaction implies that GP1 remains associated with GP2 until after
403 engagement with the target membrane. NPC1 binding to GP1 may partially serve to localize EBOV on the
404 endosomal membrane to increase the efficiency with which the fusion loop inserts into the membrane.
405 Given previous studies indicating that acidic pH does not trigger GP-mediated fusion [50,51], we speculate
406 that events downstream of the GP-membrane interaction may not be pH dependent. A recent study
407 suggested the proteolytic activity of cathepsins during the final stages of fusion [15].

408 Ca^{2+} can assist in membrane fusion through coordination by anionic residues in the fusion loop, as seen
409 for Rubella virus, MERS-CoV, SARS-CoV-1 and -2, and EBOV [14,52–55]. This may stabilize a fusion loop
410 conformation that is optimal for insertion into the membrane. In addition, Ca^{2+} coordination in the fusion
411 loop can affect the physical properties of the target membrane in a manner that promotes fusion [54].

412 Previous studies have shown that elevated Ca^{2+} can inhibit EBOV entry and GP function by an unknown
413 mechanism [12,56]. While estimates of the Ca^{2+} concentration in the late endosome vary considerably,
414 previous cell-based and *in-vitro* studies of the EBOV fusion loop or the intact GP trimer have utilized
415 concentrations in the range of 0.5-2 mM [9,28,57], which may exceed the physiological concentration
416 [58–60]. To ensure results that are comparable with the literature, we opted to maintain this precedence
417 in our experiments. The overall consistency in our results from measurements of membrane binding and
418 infectivity suggest that alternative Ca^{2+} concentrations would not affect the interpretation of our data.
419 Moreover, the titration of Ca^{2+} indicated that BMP promotes GP^{CL}-membrane binding across the
420 physiological range of concentrations.

421 The importance of anionic residues, D522 and E540, in mediating the Ca^{2+}-dependence of fusion loop-
422 membrane interaction and lipid mixing was previously reported [14]. Our findings support these
423 conclusions and confirm that residues D522 and E540 are critical mediators of the Ca^{2+}-dependence of
424 trimeric GP^{CL}-membrane interaction. The results presented here provide the additional insight that these
425 residues contribute to stabilization of the pre-fusion conformation, but their coordination of Ca^{2+} does
426 not drive large-scale GP^{CL} conformational changes. Rather, we propose that acidic pH is the primary driver
427 of GP^{CL} conformational changes that are necessary for interaction with the membrane, whereas Ca^{2+}
428 binding likely has a localized effect on the fusion loop. Structural studies of the intact trimer, performed
429 under conditions that promote membrane fusion, are needed to elucidate the GP2 structure, the relative
430 position of the GP1 domain, and the local fusion loop configuration that enables engagement with the
431 target membrane. Biophysical interrogations such as those presented here, likely involving smFRET
432 imaging with alternative fluorophore attachment sites, should guide these future studies by identifying
433 conditions that promote functional conformations and the residues that mediate their stability.

434 **Material and Methods**

435 ***Cell lines***

436 Expi293F cells (Gibco, ThermoFisher Scientific, Waltham, MA) were cultured in Expi293 expression
437 medium in an orbital shaking incubator at 37°C, 8% CO_2, 125rpm. HEK293T FirB cells, which have high
438 furin expression, were a kind gift from Dr. Theodore C. Pierson (Emerging Respiratory Virus section,
439 Laboratory of Infectious Diseases, NIH, Bethesda, MD) [61]. These cells were cultured in DMEM (Gibco,
440 ThermoFisher Scientific, Waltham, MA) with 10% cosmic calf serum (Hyclone, Cytiva Life Sciences,
441 Marlborough, MA) and 1% penicillin-streptomycin (Gibco, ThermoFisher Scientific, Waltham, MA) at 37°C,
442 5% CO_2.

443 ***Plasmids***

444 pHLsec-GPΔTM and pMAM51-GPΔmuc plasmids were obtained from Dr. Kartik Chandran's lab (Einstein
445 College of Medicine, NY). pHLsec-GPΔTM encodes EBOV (Mayinga) GP sequence (UniProt Q05320) with
446 deleted mucin-like and transmembrane domains. A T4 fibritin foldon trimerization domain and 6X-
447 histidine tag for Ni-NTA purification has been inserted into the C terminus. The A1 (*GDSLDMLEWSLM*) and
448 A4 (*DSLSMLEW*) peptides were introduced at positions 32 and 501 in GP1 and GP2, respectively, for site-
449 specific labelling of GPΔTM, as previously described [62]. pMAM51-GPΔmuc encodes full-length GP with
450 the mucin-like domain deleted and was used for all pseudovirion experiments. In both GPΔTM and
451 GPΔmuc the thermolysin cleavage site, *VNAT* at position 203, was replaced with an HRV3C protease
452 recognition site (*LEVLFQGP*) by site directed mutagenesis (Q5 site directed mutagenesis kit, New England
453 Biolabs, Ipswich, MA). All amino acid substitutions were also introduced in GPΔTM and GPΔmuc via site-
454 directed mutagenesis. pNL4.3.Luc.R-E- used in infectivity assays was obtained through the NIH AIDS
455 Reagent program (contributed by Dr. Nathaniel Landau, New York University School of Medicine) [63]. An
456 amber stop codon (TAG) in the *tat* gene was modified by site-directed mutagenesis to --TAA to prevent

457 readthrough during incorporation of TCO* for labelling of GPΔmuc. Plasmids PyIRS^{AF} and eRF1 were
458 provided by Dr. Edward Lemke (Johannes Gutenberg-University of Mainz, Germany).

459 ***Protein expression and purification***

460 For production of GPΔTM proteins (wild-type and mutants), Expi293F cells were transfected with pHLsec-
461 GPΔTM using polyethyleneimine (PEI MAX, Polysciences, Warrington, PA) at a mass ratio of 1:3 DNA:PEI
462 MAX. As previously described, a 2:1 ratio of pHLsec-GPΔTM to tagged pHLsec-GPΔTM was transfected to
463 ensure that GPΔTM trimers contained on average a single tagged protomer. The supernatants containing
464 soluble GPΔTM proteins were harvested 5 days post-transfection. The proteins were purified using Ni-
465 NTA agarose beads (Pierce, ThermoFisher Scientific, Waltham, MA). The protein was bound to the column
466 in phosphate-buffered saline (PBS) containing 10mM imidazole, followed by washing with 20mM
467 imidazole in PBS and elution in 200 mM imidazole containing PBS. Following purification, proteins were
468 exchanged to labelling buffer (20 mM HEPES, 50 mM NaCl, pH 7.5) using VivaSpin 6 concentrator
469 (Sartorius AG, Gottingen, Germany).

470 ***Labelling of GPΔTM***

471 Wild-type and mutant GPΔTM proteins were labelled with 5 µM LD650 conjugated to coenzyme A (LD650-
472 CoA; Lumidyne Technologies, New York, NY). The fluorophore was attached to the A1 and A4 peptides in
473 the tagged GPΔTM through incubation with 5 µM acyl carrier protein synthase (AcpS) in the labelling
474 buffer with 10 mM $Mg(CH_3COO)_2$ overnight at room temperature [62]. The labelled proteins were
475 subjected to overnight cleavage by exogenous furin (New England Biolabs, Ipswich, MA) at 37°C to fully
476 convert GP0 to GP1 and GP2. The processed proteins were purified by size-exclusion chromatography on
477 a Superdex 200 Increase 10/300 GL column (GE Healthcare, Chicago, IL). Purified, labelled proteins were

478 concentrated using Amicon Ultra 30K filters (MilliporeSigma, Burlington, MA), aliquoted and stored at -
479 80°C until further use. The concentration of proteins was determined using Bradford reagent.

480 ***Indirect ELISA***

481 Labelled proteins were diluted to a final concentration of 5 µg/ml in PBS and coated onto the wells of a
482 96-well polystyrene plate (Pierce™, ThermoFisher Scientific, Waltham, MA) by incubating overnight at
483 4°C. The plate was washed three times with PBST (PBS with 0.1% Tween-20) followed by blocking with 5%
484 skim milk in PBST for 3h at room temperature. The blocking solution was removed, and the plate was
485 again washed twice with PBST. Proteins were probed with KZ52 antibody [37,62] at a dilution of 1:1000
486 overnight at 4°C. The plate was then washed and incubated with horseradish peroxidase-conjugated anti-
487 human IgG (Invitrogen™, ThermoFisher Scientific, Waltham, MA) at a dilution of 1:2000 for 2h at room
488 temperature. After washing the plate four times with PBST, TMB solution (3,3',5,5'-tetramethylbenzidine;
489 ThermoFisher Scientific, Waltham, MA) was added to each well, incubated for 15 min, followed by
490 addition of an equal volume of 2M sulphuric acid. The optical density was immediately read at 450 nm in
491 a Synergy H1 microplate reader (BioTek, Winooski, VT).

492 ***Liposome preparation***

493 The following lipids were used for liposome preparation: POPC (1-palmitoyl-2-oleoyl-glycero-3-
494 phosphocholine), POPS (1-palmitoyl-2-oleoyl-sn-glycero-3-phospho-L-serine (sodium salt)), BMP
495 (bis(monooleoylglycero)phosphate (S,R Isomer)) and cholesterol (all from Avanti Polar lipids, Alabaster,
496 AL). Stock solution of lipids (10 mg/ml) were diluted at desired ratios in chloroform to obtain a final total
497 lipid concentration of 1 mM. A lipid film was formed in a glass vial by evaporating the chloroform under a
498 steady stream of Argon gas. Residual chloroform was removed by incubating the lipid film overnight under
499 vacuum. Lipids were rehydrated with 5 mM HEPES, 10 mM MES and 150 mM NaCl, pH 7.5, for 1 hour at

500 room temperature. The lipid suspension was vortexed 5-7 times in 10 sec pulses followed by 10 freeze-
501 thaw cycles with liquid nitrogen. Liposomes were formed by extruding the lipid solution 37 times through
502 a 100 nm polycarbonate membrane (Whatman® Nucleopore™ track-etched membrane) in a mini-
503 extruder (Avanti Polar Lipids, Alabaster, AL). The size of liposomes was verified using dynamic light
504 scattering (Zetasizer Nano, Malvern Panalytical, Malvern, UK). The liposomes were stored at 4°C and used
505 within a week.

506 ***HRV3C cleavage***

507 Thermolysin is commonly used to remove the glycan cap from GP1 in place of the endosomal cathepsin
508 proteases [64]. However, this led to removal of the fluorophore from labelled GPΔTM. To alleviate this
509 off-target effect of thermolysin, the thermolysin cleavage site was replaced with the HRV3C protease
510 recognition sequence. The glycan cap was thus removed from GPΔTM and pseudovirions with GPΔmuc
511 through incubation with HRV3C protease (Pierce™, ThermoFisher Scientific, Waltham, MA) at 10°C for 16
512 hr, which left the fluorescent labelling intact (**Figure S2A**). Cleavage of LD650-labelled GPΔTM was verified
513 by in-gel fluorescence imaging of uncleaved and cleaved protein on a 4-20% polyacrylamide using a
514 ChemiDoc™ MP imaging system (Bio-Rad, Hercules, CA) followed by Coomassie staining. In a pseudovirion
515 infectivity assay, introduction of the HRV3C sequence left GP 85% functional as compared to wild-type GP
516 (**Figure S2B**).

517 ***Fluorescence correlation spectroscopy***

518 For membrane binding studies, liposomes (500 µM total lipid) were incubated with 5 nM labelled GP^{CL}in
519 5 mM HEPES, 10 mM MES, 150 mM NaCl (pH 7.5 or 5.5). For experiments performed in the absence of
520 Ca^{2+}, 1mM EDTA was included to chelate any Ca^{2+} already bound to GP^{CL}. Otherwise, the indicated
521 concentration of $CaCl_2$ (0-1mM) was included in the incubation. The liposome-GP^{CL} mixture was incubated

522 at 37°C for 20 min to allow binding. For experiments performed at pH 5.5, the liposome mixture was
523 acidified with 1 M HCl prior to addition of GP^{CL}. FCS experiments were performed by dropping 50 µL of
524 the liposome-GP^{CL} mixture onto a coverslip (No. 1.5 Thorlabs, Newton, NJ). To prevent sticking of the
525 protein-membrane complex to the glass surface, coverslips were plasma-cleaned followed by coating with
526 10% polyethylene glycol (PEG-8000, Promega, Madison, WI). 100 autocorrelation curves, 5 sec each in
527 length, were recorded at room temperature using a 638 nm laser in a CorTector SX100 (LightEdge
528 Technologies Ltd., Zhongshan City, China). The curves were fitted to the following model for two species
529 diffusing in three dimensions with triplet blinking [25,65,66]:

530 $G(\tau) = G_{triplet}(\tau).\, G_{complex}(\tau)$, where

531 $G_{triplet}(\tau) = 1 - T + T \cdot e^{\frac{\tau}{\tau_{triplet}}}$, and

532 $$G_{complex}(\tau) = \frac{1}{N}\left(f \cdot \left[1 + \frac{\tau}{\tau_{protein}}\right]^{-1} \left[1 + \frac{\tau}{s^2 \tau_{protein}}\right]^{-1/2} + \alpha \cdot (1 - f)\right.$$

533 $$\left. \cdot \left[1 + \frac{\tau}{\tau_{liposome}}\right]^{-1} \left[1 + \frac{\tau}{s^2 \tau_{liposome}}\right]^{-1/2} \right)$$

534

535 where, *N* is the number of molecules in the confocal volume, f is the fraction of free protein, α is the
536 average brightness of the protein-liposome complex, $\tau_{protein}$ is the diffusion time of free protein,
537 $\tau_{liposome}$ is the diffusion time of the liposome, and *s* is the structural parameter, which reflects the
538 dimensions of the confocal volume. The diffusion times, $\tau_{protein}$ and $\tau_{liposome}$ were calculated by fitting
539 the autocorrelation curves of GPΔTM and liposomes (labelled with 40nM DiD) separately to single species
540 diffusion models. The values of *s* and $\tau_{protein}$ were kept constant to calculate the fraction of free and

541 bound protein for all samples. Due to polydispersity of liposomes and fast photophysical dynamics of
542 triplet blinking, $\tau_{liposome}$ and $\tau_{triplet}$ were allowed to vary during fitting. The analysis was carried out in
543 MATLAB (MathWorks, Natick, MA) using a non-linear least-square curve fitting algorithm. All values were
544 averaged over three independent experiments. Two-tailed, independent Student's T-tests were
545 performed to calculate the statistical significance between mutations under the conditions tested (α =
546 0.05).

547 ***Western blotting***

548 All proteins and pseudovirions were run on 4-20% denaturing polyacrylamide gels (Bio-Rad, Hercules, CA)
549 and transferred to nitrocellulose membrane using Trans-blot Turbo (Bio-Rad, Hercules, CA). Membranes
550 were rinsed with PBST, blocked with 5% skim milk in PBST for 1 h followed by probing of GP and p24 with
551 monoclonal antibody (mAb) H3C8 at a dilution of 1:1000, [67] and mouse mAB B1217M at a dilution of
552 1:2000 (Genetex, Irvine, CA), respectively. The mAb H3C8 was humanized by cloning its variable heavy
553 and light chain fragments in human IgG expression vectors obtained from Dr. Michel Nussenzwieg (The
554 Rockefeller University). Membranes were washed three times with PBST, incubated with horseradish
555 peroxidase-conjugated anti-human IgG (Invitrogen™, ThermoFisher, Waltham, MA) and anti-mouse IgG
556 (ThermoFisher, Waltham, MA) for 1 h at room temperature and developed with SuperSignal™ West Pico
557 PLUS chemiluminescent substrate (ThermoFisher Scientific, Waltham, MA).

558 ***Infectivity assay***

559 Infectivity of VSV pseudovirions containing wild-type GPΔmuc was compared to pseudovirions containing
560 GPΔmuc^{HRV3C} via flow cytometry [68]. HEK293T cells were transfected with GPΔmuc and GPΔmuc^{HRV3C}
561 plasmid using polyethyleneimine (PEI MAX, Polysciences, Warrington, PA) at a mass ratio of 1:3 PEI
562 MAX:DNA. Cells were transduced with VSVΔG-GFP-VSVG pseudovirions 24 h after transfection.

563 Supernatants containing VSVΔG-GFP-GPΔmuc and VSVΔG-GFP-GPΔmuc^{HRV3C} were collected 24 h post-
564 transduction and filtered through 0.45 µm filter. As a negative control, bald particles were generated by
565 transducing cells not expressing GPΔmuc. Vero cells were infected with VSV pseudovirions through
566 incubation at 37°C for 1 h with gentle agitation every 15min to allow even spread of pseudovirions. Fresh
567 media was added, and infection was allowed to proceed for five more hours. Cells were trypsinized and
568 assayed for expression of GFP using a flow cytometer (MACSQuant Analyzer 1.0). The results were
569 averaged across technical replicates and standard error was calculated from biological replicates.

570 To assess infectivity of GPΔmuc^{HRV3C} mutants, pseudovirions with luciferase-expressing HIV-1 core were
571 produced. Plasmids pMAM51-GPΔmuc^{HRV3C} and pNL4.3.Luc.R-E- were co-transfected at a ratio of 1:5 in
572 HEK 293T FirB cells. Pseudovirions were harvested 24 h post-transfection by collecting the supernatant,
573 passing through a 0.45 µm filter, and layering on 10% sucrose in PBS solution followed by
574 ultracentrifugation at 25000 rpm for 2 h at 4°C. After resuspension of the pellet in PBS, particles were
575 analyzed by western blot. The virions were cleaved with HRV3C to remove the glycan cap as above,
576 incubated with Vero cells for 5 h at 37°C, followed by replacement of growth media. After 48 h, cells were
577 lysed with Glo Lysis Buffer (Promega, Madison, WI) for 5 min at room temperature. Luciferase activity was
578 recorded by mixing equal volumes of cell lysate and Steady Glo Reagent (Promega, Madison, WI) and
579 reading in a Synergy H1 plate reader (Biotek, Winooski, VT). The luminescence was normalized to
580 expression of GP for each sample. Bald pseudovirions containing only pNL4.3.Luc.R-E- were used as a
581 negative control.

582 ***Pseudovirion production and fluorescent labelling***

583 To facilitate attachment of fluorophores to GP on the surface of pseudovirions for smFRET imaging, the
584 non-natural amino acid TCO* (SiChem GmbH, Bremen, Germany) was introduced at positions 501 and 610
585 through amber stop codon suppression (GP*) (**Figure 2B**) (Nikić et al., 2016). Pseudovirions were produced

586 by transfecting HEK293T FirB cells with pMAM51-GPΔmuc^{HRV3C} plasmids with and without amber stop
587 codons at a 1:1 ratio, which equated to an excess of GP protein over GP*. This ratio was optimized to
588 ensure that the pseudovirions rarely contained more than a single GP* protomer per particle. A plasmid
589 encoding HIV-1 GagPol was also transfected to provide the pseudovirion core. To increase the efficiency
590 of amber codon readthrough, plasmids eRF1 and PyIRS^{AF} were also included in transfection [12,69]. The
591 supernatant containing pseudovirions was harvested 48 h post-transfection, filtered through a 0.45 µm
592 mixed cellulose ester membrane and layered onto 10% sucrose (in PBS) solution. The pseudovirions were
593 pelleted by ultracentrifugation at 25000 rpm for 2 h at 4°C. Pseudovirions were resuspended in 500 µL
594 PBS and incubated with 500 nM Cy3- and Cy5-tetrazine (Jena Biosciences, Jena, Germany) for 30 min at
595 room temperature. 60 µM DSPE-PEG2000 biotin (Avanti Polar Lipids, Alabaster, AL) was added to the
596 labelling reaction and incubated for another 30 min at room temperature with gentle mixing. The labelling
597 reaction was layered on a 6-30% OptiPrep (Sigma-Aldrich, MilliporeSigma, Burlington, MA) density
598 gradient and ultracentrifuged at 35000 rpm for 1 h at 4°C. Labelled pseudovirions were collected,
599 aliquoted, and analyzed by western blot.

600 ***smFRET imaging assay and data analysis***

601 All smFRET experiments were performed following removal of the glycan cap from GP. Labelled and glycan
602 cap-cleaved pseudovirions were immobilized on streptavidin-coated quartz slides and imaged on a wide-
603 field prism-based TIRF microscope [70]. Imaging was performed in the same buffer used for the
604 membrane binding assay (5 mM HEPES, 10 mM MES, 150 mM NaCl [pH 7.5 or 5.5]). To study the effect of
605 Ca^{2+}, the buffer was supplemented with 1 mM $CaCl_2$. smFRET data was acquired at room temperature at
606 25 frames/sec using the MicroManager microscope control software (micromanager.org). Analysis of
607 smFRET data was performed using the SPARTAN software package
608 (https://www.scottcblanchardlab.com/software) [71] in Matlab (MathWorks, Natick, MA). smFRET

609 trajectories were selected according to the following criteria: acceptor fluorescence intensity greater than
610 35; FRET was detectable for at least 15 frames prior to photobleaching; correlation coefficient between
611 donor and acceptor fluorescence traces was less than -0.4; signal-to-noise ratio was greater than 10; and
612 background fluorescence was less than 50. Trajectories that met these criteria were further verified
613 manually and fitted to a 5-state linear hidden Markov model (including a zero-FRET state) using maximum
614 point likelihood (MPL) algorithm implemented in SPARTAN [72]. The 5-state linear model was chosen
615 based on the Akaike Information Criterium (AIC) and the Bayesian Inference Criterium (BIC) (**Figure S4**)
616 [73,74]. Several models were initially considered with varying numbers of model parameters and
617 topology. The 5-state linear model minimized both the AIC and BIC criteria relative to the models
618 considered and was thus chosen for analysis. The idealizations from total number of traces for each
619 sample were used to calculate the occupancies in different FRET states and construct the FRET histograms
620 and transition density plots (TDPs).

621 ***MD simulations***

622 A model of trimeric GP^{CL} was generated from atomic coordinates determined through x-ray
623 crystallography (PDB accession: 5HJ3) [31]. The model included residues 32-188 of GP1 and 502-598 of
624 GP2. The protein components of the models were parameterized with the CHARMM36m forcefield using
625 CHARMM-GUI. The systems were charge neutralized and solvated with the TIP3P explicit solvent model.
626 The solvated proteins were energy minimized for 0.1 ns, followed by equilibration using a stepwise
627 protocol [75]. Briefly, the protein backbone was harmonically constrained, with the constraints being
628 released stepwise over 4 0.3-ns intervals. Equilibration was run in the NPT ensemble with temperature
629 maintained at 310 K and pressure maintained at 1 atm using the Langevin thermostat and the Nose-
630 Hoover Langevin barostat, respectively. Electrostatics were calculated using the Particle Mesh Ewald
631 algorithm. Constant-pH MD simulations were run using the *cph* module in NAMD v2.14 on the SCI cluster

632 at UMass Chan Medical School [32]. Titrations were simulated in triplicate with 14 pH points ranging from
633 4.2 to 7.5. Protonation switches were attempted every 1 ps with switch times of 20 ps for 1000 cycles,
634 yielding a total simulation time of 21 ns for each of three replicas. Inherent pKa values were assigned with
635 PropKa. The results of the constant-pH simulations were analyzed using the *cphanalyze* program in the
636 *pynamd* analysis package. Apparent pK_as and Hill coefficients were determined by linear fitting in Matlab.
637 Equilibrium MD simulations were run for 250 ns in the NPT ensemble using a GPU-accelerated installation
638 of NAMD v3.0b2. on the SCI cluster at UMass Chan Medical School. Trajectories were visualized in VMD
639 and analyzed using the Tcl scripting interface.

640 **Acknowledgements**

641 The authors would like to thank Dr. Gang Han (UMass Chan Medical School, Worcester, MA) for assistance
642 with dynamic light scattering. This work was supported by NIH grants R01AI174645 and R01GM143773 to
643 J.B.M, and R01AI148784 to J.L.

644 **References**

645 1. Salata C, Calistri A, Alvisi G, Celestino M, Parolin C, Palù G. Ebola Virus Entry: From Molecular
646 Characterization to Drug Discovery. Viruses. 2019;11: 274. doi:10.3390/v11030274

647 2. Lee JE, Fusco ML, Hessell AJ, Oswald WB, Burton DR, Saphire EO. Structure of the Ebola virus
648 glycoprotein bound to an antibody from a human survivor. Nature. 2008;454: 177–182.
649 doi:10.1038/nature07082

650 3. Nanbo A, Imai M, Watanabe S, Noda T, Takahashi K, Neumann G, et al. Ebolavirus Is Internalized into
651 Host Cells via Macropinocytosis in a Viral Glycoprotein-Dependent Manner. Plos Pathog. 2010;6:
652 e1001121. doi:10.1371/journal.ppat.1001121

653 4. Mulherkar N, Raaben M, Torre JC de la, Whelan SP, Chandran K. The Ebola virus glycoprotein
654 mediates entry via a non-classical dynamin-dependent macropinocytic pathway. Virology. 2011;419: 72–
655 83. doi:10.1016/j.virol.2011.08.009

656 5. Carette JE, Raaben M, Wong AC, Herbert AS, Obernosterer G, Mulherkar N, et al. Ebola virus entry
657 requires the cholesterol transporter Niemann-Pick C1. Nature. 2011;477: 340–343.
658 doi:10.1038/nature10348

659 6. Chandran K, Sullivan NJ, Felbor U, Whelan SP, Cunningham JM. Endosomal Proteolysis of the Ebola
660 Virus Glycoprotein Is Necessary for Infection. Science. 2005;308: 1643–1645.
661 doi:10.1126/science.1110656

662 7. Côté M, Misasi J, Ren T, Bruchez A, Lee K, Filone CM, et al. Small molecule inhibitors reveal Niemann–
663 Pick C1 is essential for Ebola virus infection. Nature. 2011;477: 344–348. doi:10.1038/nature10380

664 8. Miller EH, Obernosterer G, Raaben M, Herbert AS, Deffieu MS, Krishnan A, et al. Ebola virus entry
665 requires the host-programmed recognition of an intracellular receptor. Embo J. 2012;31: 1947–1960.
666 doi:10.1038/emboj.2012.53

667 9. Fénéant L, Wijs KMS, Nelson EA, White JM. An exploration of conditions proposed to trigger the Ebola
668 virus glycoprotein for fusion. Plos One. 2019;14: e0219312. doi:10.1371/journal.pone.0219312

669 10. Saeed MF, Kolokoltsov AA, Albrecht T, Davey RA. Cellular Entry of Ebola Virus Involves Uptake by a
670 Macropinocytosis-Like Mechanism and Subsequent Trafficking through Early and Late Endosomes. Plos
671 Pathog. 2010;6: e1001110. doi:10.1371/journal.ppat.1001110

672 11. Brecher M, Schornberg KL, Delos SE, Fusco ML, Saphire EO, White JM. Cathepsin Cleavage
673 Potentiates the Ebola Virus Glycoprotein To Undergo a Subsequent Fusion-Relevant Conformational
674 Change. J Virol. 2012;86: 364–372. doi:10.1128/jvi.05708-11

675 12. Das DK, Bulow U, Diehl WE, Durham ND, Senjobe F, Chandran K, et al. Conformational changes in the
676 Ebola virus membrane fusion machine induced by pH, Ca2+, and receptor binding. Plos Biol. 2020;18:
677 e3000626. doi:10.1371/journal.pbio.3000626

678 13. Sakurai Y, Kolokoltsov AA, Chen C-C, Tidwell MW, Bauta WE, Klugbauer N, et al. Two-pore channels
679 control Ebola virus host cell entry and are drug targets for disease treatment. Science. 2015;347: 995–
680 998. doi:10.1126/science.1258758

681 14. Nathan L, Lai AL, Millet JK, Straus MR, Freed JH, Whittaker GR, et al. Calcium Ions Directly Interact
682 with the Ebola Virus Fusion Peptide To Promote Structure–Function Changes That Enhance Infection.
683 ACS Infectious Diseases. 2020;6: 250–260. doi:10.1021/acsinfecdis.9b00296

684 15. Odongo L, Habtegebrael BH, Kiessling V, White JM, Tamm LK. A novel in vitro system of supported
685 planar endosomal membranes (SPEMs) reveals an enhancing role for cathepsin B in the final stage of
686 Ebola virus fusion and entry. Microbiol Spectr. 2023;11: e01908-23. doi:10.1128/spectrum.01908-23

687 16. Lee J, Gregory SM, Nelson EA, White JM, Tamm LK. The Roles of Histidines and Charged Residues as
688 Potential Triggers of a Conformational Change in the Fusion Loop of Ebola Virus Glycoprotein. Plos One.
689 2016;11: e0152527. doi:10.1371/journal.pone.0152527

690 17. Mazzon M, Mercer J. Lipid interactions during virus entry and infection. Cell Microbiol. 2014;16:
691 1493–1502. doi:10.1111/cmi.12340

692 18. Urade R, Hayashi Y, Kito M. Endosomes differ from plasma membranes in the phospholipid
693 molecular species composition. Biochimica Et Biophysica Acta Bba - Biomembr. 1988;946: 151–163.
694 doi:10.1016/0005-2736(88)90468-3

695 19. Hullin-Matsuda F, Taguchi T, Greimel P, Kobayashi T. Lipid compartmentalization in the endosome
696 system. Semin Cell Dev Biol. 2014;31: 48–56. doi:10.1016/j.semcdb.2014.04.010

697 20. Zaitseva E, Yang S-T, Melikov K, Pourmal S, Chernomordik LV. Dengue Virus Ensures Its Fusion in Late
698 Endosomes Using Compartment-Specific Lipids. Plos Pathog. 2010;6: e1001131.
699 doi:10.1371/journal.ppat.1001131

700 21. Markosyan RM, Marin M, Zhang Y, Cohen FS, Melikyan GB. The late endosome-resident lipid
701 bis(monoacylglycero)phosphate is a cofactor for Lassa virus fusion. Plos Pathog. 2021;17: e1009488.
702 doi:10.1371/journal.ppat.1009488

703 22. Bitto D, Halldorsson S, Caputo A, Huiskonen JT. Low pH and Anionic Lipid-dependent Fusion of
704 Uukuniemi Phlebovirus to Liposomes*. J Biol Chem. 2016;291: 6412–6422.
705 doi:10.1074/jbc.m115.691113

706 23. Matos PM, Marin M, Ahn B, Lam W, Santos NC, Melikyan GB. Anionic lipids are required for vesicular
707 stomatitis virus G protein-mediated single particle fusion with supported lipid bilayers. J Biological
708 Chem. 2013;288: 12416–25. doi:10.1074/jbc.m113.462028

709 24. Nour AM, Li Y, Wolenski J, Modis Y. Viral Membrane Fusion and Nucleocapsid Delivery into the
710 Cytoplasm are Distinct Events in Some Flaviviruses. Plos Pathog. 2013;9: e1003585.
711 doi:10.1371/journal.ppat.1003585

712 25. Betaneli V, Mücksch J, Schwille P. Lipid-Protein Interactions, Methods and Protocols. Methods Mol
713 Biology. 2019;2003: 415–447. doi:10.1007/978-1-4939-9512-7_18

714 26. Durham ND, Howard AR, Govindan R, Senjobe F, Fels JM, Diehl WE, et al. Real-Time Analysis of
715 Individual Ebola Virus Glycoproteins Reveals Pre-Fusion, Entry-Relevant Conformational Dynamics.
716 Viruses. 2020;12: 103. doi:10.3390/v12010103

717 27. Bissig C, Gruenberg J. Lipid Sorting and Multivesicular Endosome Biogenesis. Csh Perspect Biol.
718 2013;5: a016816. doi:10.1101/cshperspect.a016816

719 28. Das DK, Bulow U, Diehl WE, Durham ND, Senjobe F, Chandran K, et al. Conformational changes in the
720 Ebola virus membrane fusion machine induced by pH, Ca2+, and receptor binding. Plos Biol. 2020;18:
721 e3000626. doi:10.1371/journal.pbio.3000626

722 29. Nikić I, Girona GE, Kang JH, Paci G, Mikhaleva S, Koehler C, et al. Debugging Eukaryotic Genetic Code
723 Expansion for Site-Specific Click-PAINT Super-Resolution Microscopy. Angewandte Chemie Int Ed.
724 2016;55: 16172 16176. doi:10.1002/anie.201608284

725 30. Zhao Y, Ren J, Harlos K, Jones DM, Zeltina A, Bowden TA, et al. Toremifene interacts with and
726 destabilizes the Ebola virus glycoprotein. Nature. 2016;535: 169–172. doi:10.1038/nature18615

727 31. Bornholdt ZA, Ndungo E, Fusco ML, Bale S, Flyak AI, Crowe JE, et al. Host-Primed Ebola Virus GP
728 Exposes a Hydrophobic NPC1 Receptor-Binding Pocket, Revealing a Target for Broadly Neutralizing
729 Antibodies. Mbio. 2015;7: e02154 15. doi:10.1128/mbio.02154-15

730 32. Radak BK, Chipot C, Suh D, Jo S, Jiang W, Phillips JC, et al. Constant-pH Molecular Dynamics
731 Simulations for Large Biomolecular Systems. J Chem Theory Comput. 2017;13: 5933–5944.
732 doi:10.1021/acs.jctc.7b00875

733 33. Lee J, Gregory SM, Nelson EA, White JM, Tamm LK. The Roles of Histidines and Charged Residues as
734 Potential Triggers of a Conformational Change in the Fusion Loop of Ebola Virus Glycoprotein. Plos One.
735 2016;11: e0152527. doi:10.1371/journal.pone.0152527

736 34. Gregory SM, Larsson P, Nelson EA, Kasson PM, White JM, Tamm LK. Ebolavirus entry requires a
737 compact hydrophobic fist at the tip of the fusion loop. J Virol. 2014;88: 6636 6649.
738 doi:10.1128/jvi.00396-14

739 35. Manicassamy B, Wang J, Jiang H, Rong L. Comprehensive analysis of ebola virus GP1 in viral entry. J
740 Virol. 2005;79: 4793 4805. doi:10.1128/jvi.79.8.4793-4805.2005

741 36. Brindley MA, Hughes L, Ruiz A, McCray PB, Sanchez A, Sanders DA, et al. Ebola Virus Glycoprotein 1:
742 Identification of Residues Important for Binding and Postbinding Events. J Virol. 2007;81: 7702–7709.
743 doi:10.1128/jvi.02433-06

744 37. Maruyama T, Rodriguez LL, Jahrling PB, Sanchez A, Khan AS, Nichol ST, et al. Ebola Virus Can Be
745 Effectively Neutralized by Antibody Produced in Natural Human Infection. J Virol. 1999;73: 6024–6030.
746 doi:10.1128/jvi.73.7.6024-6030.1999

747 38. Lee JE, Fusco ML, Hessell AJ, Oswald WB, Burton DR, Saphire EO. Structure of the Ebola virus
748 glycoprotein bound to an antibody from a human survivor. Nature. 2008;454: 177–182.
749 doi:10.1038/nature07082

750 39. Matsuo H, Chevallier J, Mayran N, Blanc IL, Ferguson C, Fauré J, et al. Role of LBPA and Alix in
751 Multivesicular Liposome Formation and Endosome Organization. Science. 2004;303: 531–534.
752 doi:10.1126/science.1092425

753 40. Kobayashi T, Beuchat M-H, Chevallier J, Makino A, Mayran N, Escola J-M, et al. Separation and
754 Characterization of Late Endosomal Membrane Domains*. J Biol Chem. 2002;277: 32157–32164.
755 doi:10.1074/jbc.m202838200

756 41. Mannsverk S, Giraldo AMV, Kasson PM. Influenza Virus Membrane Fusion Is Promoted by the
757 Endosome-Resident Phospholipid Bis(monoacylglycero)phosphate. J Phys Chem B. 2022;126: 10445–
758 10451. doi:10.1021/acs.jpcb.2c06642

759 42. Düzgüne§ N, Nir S, Wilschut J, Bentz J, Newton C, Portis A, et al. Calcium- and magnesium-induced
760 fusion of mixed phosphatidylserine/phosphatidylcholine vesicles: Effect of ion binding. J Membr Biol.
761 1981;59: 115–125. doi:10.1007/bf01875709

762 43. Melcrová A, Pokorna S, Pullanchery S, Kohagen M, Jurkiewicz P, Hof M, et al. The complex nature of
763 calcium cation interactions with phospholipid bilayers. Sci Rep-uk. 2016;6: 38035.
764 doi:10.1038/srep38035

765 44. Martín-Molina A, Rodríguez-Beas C, Faraudo J. Effect of calcium and magnesium on
766 phosphatidylserine membranes: experiments and all-atomic simulations. Biophys J. 2012;102: 2095–
767 103. doi:10.1016/j.bpj.2012.03.009

768 45. Alsabeeh N, Chausse B, Kakimoto PA, Kowaltowski AJ, Shirihai O. Cell culture models of fatty acid
769 overload: Problems and solutions. Biochim Biophys acta Mol cell Biol lipids. 2017;1863: 143–151.
770 doi:10.1016/j.bbalip.2017.11.006

771 46. Kobayashi T, Beuchat M-H, Chevallier J, Makino A, Mayran N, Escola J-M, et al. Separation and
772 Characterization of Late Endosomal Membrane Domains*. J Biol Chem. 2002;277: 32157–32164.
773 doi:10.1074/jbc.m202838200

774 47. UPHOFF A, HERMANSSON M, HAIMI P, SOMERHARJU P. Medical Applications of Mass Spectrometry.
775 Part III: Biomol. 2008; 223–249. doi:10.1016/b978-044451980-1.50013-6

776 48. Caffrey M, Lavie A. pH-Dependent Mechanisms of Influenza Infection Mediated by Hemagglutinin.
777 Frontiers Mol Biosci. 2021;8: 777095. doi:10.3389/fmolb.2021.777095

778 49. Harrison JS, Higgins CD, O'Meara MJ, Koellhoffer JF, Kuhlman BA, Lai JR. Role of Electrostatic
779 Repulsion in Controlling pH-Dependent Conformational Changes of Viral Fusion Proteins. Structure.
780 2013;21: 1085–1096. doi:10.1016/j.str.2013.05.009

781 50. Fénéant L, Wijs KMS, Nelson EA, White JM. An exploration of conditions proposed to trigger the
782 Ebola virus glycoprotein for fusion. Plos One. 2019;14: e0219312. doi:10.1371/journal.pone.0219312

783 51. Markosyan RM, Miao C, Zheng Y-M, Melikyan GB, Liu S-L, Cohen FS. Induction of Cell-Cell Fusion by
784 Ebola Virus Glycoprotein: Low pH Is Not a Trigger. Basler CF, editor. Plos Pathog. 2016;12: e1005373.
785 doi:10.1371/journal.ppat.1005373

786 52. Dubé M, Rey FA, Kielian M. Rubella Virus: First Calcium-Requiring Viral Fusion Protein. Plos Pathog.
787 2014;10: e1004530. doi:10.1371/journal.ppat.1004530

788 53. Singh P, Mukherji S, Basak S, Hoffmann M, Das DK. Dynamic Ca2+ sensitivity stimulates the evolved
789 SARS-CoV-2 spike strain-mediated membrane fusion for enhanced entry. Cell Reports. 2022;39: 110694.
790 doi:10.1016/j.celrep.2022.110694

791 54. Lai AL, Millet JK, Daniel S, Freed JH, Whittaker GR. The SARS-CoV Fusion Peptide Forms an Extended
792 Bipartite Fusion Platform that Perturbs Membrane Order in a Calcium-Dependent Manner. J Mol Biol.
793 2017;429: 3875–3892. doi:10.1016/j.jmb.2017.10.017

794 55. Straus MR, Tang T, Lai AL, Flegel A, Bidon M, Freed JH, et al. Ca 2+ Ions Promote Fusion of Middle
795 East Respiratory Syndrome Coronavirus with Host Cells and Increase Infectivity. J Virol. 2020;94.
796 doi:10.1128/jvi.00426-20

797 56. Johansen LM, Brannan JM, Delos SE, Shoemaker CJ, Stossel A, Lear C, et al. FDA-Approved Selective
798 Estrogen Receptor Modulators Inhibit Ebola Virus Infection. Sci Transl Med. 2013;5: 190ra79.
799 doi:10.1126/scitranslmed.3005471

800 57. Nathan L, Lai AL, Millet JK, Straus MR, Freed JH, Whittaker GR, et al. Calcium Ions Directly Interact
801 with the Ebola Virus Fusion Peptide To Promote Structure–Function Changes That Enhance Infection.
802 ACS Infectious Diseases. 2020;6: 250–260. doi:10.1021/acsinfecdis.9b00296

803 58. Christensen KA, Myers JT, Swanson JA. pH-dependent regulation of lysosomal calcium in
804 macrophages. J Cell Sci. 2002;115: 599–607.

805 59. Gerasimenko JV, Tepikin AV, Petersen OH, Gerasimenko OV. Calcium uptake via endocytosis with
806 rapid release from acidifying endosomes. Curr Biol. 1998;8: 1335–1338. doi:10.1016/s0960-
807 9822(07)00565-9

808 60. Albrecht T, Zhao Y, Nguyen TH, Campbell RE, Johnson JD. Fluorescent biosensors illuminate calcium
809 levels within defined beta-cell endosome subpopulations. Cell Calcium. 2015;57: 263–274.
810 doi:10.1016/j.ceca.2015.01.008

811 61. Mukherjee S, Dowd KA, Manhart CJ, Ledgerwood JE, Durbin AP, Whitehead SS, et al. Mechanism and
812 significance of cell type-dependent neutralization of flaviviruses. J Virol. 2014;88: 7210–20.
813 doi:10.1128/jvi.03690-13

814 62. Durham ND, Howard AR, Govindan R, Senjobe F, Fels JM, Diehl WE, et al. Real-Time Analysis of
815 Individual Ebola Virus Glycoproteins Reveals Pre-Fusion, Entry-Relevant Conformational Dynamics.
816 Viruses. 2020;12: 103. doi:10.3390/v12010103

817 63. He J, Choe S, Walker R, Marzio PD, Morgan DO, Landau NR. Human immunodeficiency virus type 1
818 viral protein R (Vpr) arrests cells in the G2 phase of the cell cycle by inhibiting p34cdc2 activity. J Virol.
819 1995;69: 6705–11. doi:10.1128/jvi.69.11.6705-6711.1995

820 64. Schornberg K, Matsuyama S, Kabsch K, Delos S, Bouton A, White J. Role of endosomal cathepsins in
821 entry mediated by the Ebola virus glycoprotein. J Virol. 2006;80: 4174 4178. doi:10.1128/jvi.80.8.4174-
822 4178.2006

823 65. Rhoades E, Ramlall TF, Webb WW, Eliezer D. Quantification of α-Synuclein Binding to Lipid Vesicles
824 Using Fluorescence Correlation Spectroscopy. Biophys J. 2006;90: 4692–4700.
825 doi:10.1529/biophysj.105.079251

826 66. Ducas VC, Rhoades E. Quantifying Interactions of β-Synuclein and γ-Synuclein with Model
827 Membranes. J Mol Biol. 2012;423: 528–539. doi:10.1016/j.jmb.2012.08.008

828 67. Ou W, Delisle J, Konduru K, Bradfute S, Radoshitzky SR, Retterer C, et al. Development and
829 characterization of rabbit and mouse antibodies against ebolavirus envelope glycoproteins. J Virol
830 Methods. 2010;174: 99–109. doi:10.1016/j.jviromet.2011.04.003

831 68. Whitt MA. Generation of VSV pseudotypes using recombinant ΔG-VSV for studies on virus entry,
832 identification of entry inhibitors, and immune responses to vaccines. J Virol Methods. 2010;169: 365–
833 374. doi:10.1016/j.jviromet.2010.08.006

834 69. Nikić I, Girona GE, Kang JH, Paci G, Mikhaleva S, Koehler C, et al. Debugging Eukaryotic Genetic Code
835 Expansion for Site-Specific Click-PAINT Super-Resolution Microscopy. Angew Chem Int Ed. 2016;55:
836 16172–16176. doi:10.1002/anie.201608284

837 70. Blakemore RJ, Burnett C, Swanson C, Kharytonchyk S, Telesnitsky A, Munro JB. Stability and
838 conformation of the dimeric HIV-1 genomic RNA 5'UTR. Biophys J. 2021;120: 4874–4890.
839 doi:10.1016/j.bpj.2021.09.017

840 71. Juette MF, Terry DS, Wasserman MR, Altman RB, Zhou Z, Zhao H, et al. Single-molecule imaging of
841 non-equilibrium molecular ensembles on the millisecond timescale. Nat Methods. 2016;13: 341–344.
842 doi:10.1038/nmeth.3769

843 72. Qin F, Auerbach A, Sachs F. A Direct Optimization Approach to Hidden Markov Modeling for Single
844 Channel Kinetics. Biophys J. 2000;79: 1915–1927. doi:10.1016/s0006-3495(00)76441-1

845 73. Akaike H. A new look at the statistical model identification. Ieee T Automat Contr. 1974;19: 716–723.
846 doi:10.1109/tac.1974.1100705

847 74. Schwarz G. Estimating the Dimension of a Model. Ann Statistics. 1978;6.
848 doi:10.1214/aos/1176344136

849 75. Shi L, Quick M, Zhao Y, Weinstein H, Javitch JA. The Mechanism of a Neurotransmitter:Sodium
850 Symporter—Inward Release of Na+ and Substrate Is Triggered by Substrate in a Second Binding Site. Mol
851 Cell. 2008;30: 667–677. doi:10.1016/j.molcel.2008.05.008

852

853

854 **Figures and Figure Captions**

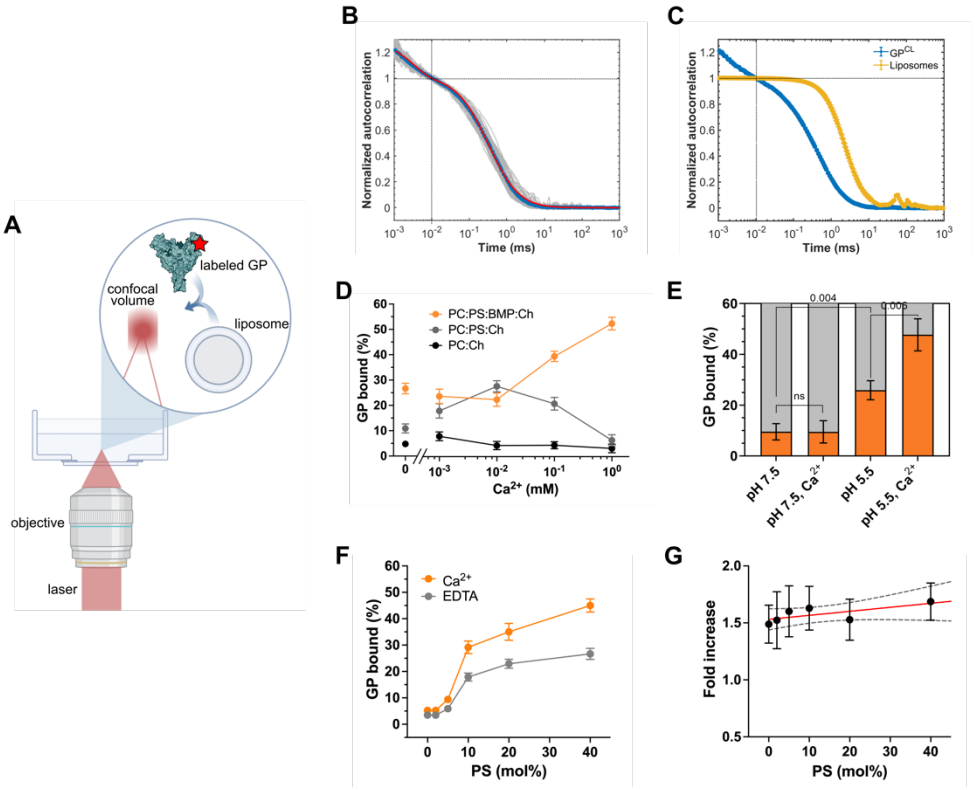

855

856 **Figure 1. Anionic phospholipids and Ca^{2+} promote GP^{CL}-membrane interaction.** (**A**) Experimental setup
857 of FCS assay for quantifying GP-membrane interactions. A confocal spot is positioned in a dilute solution
858 of Cy5-labelled GP^{CL} with or without liposomes. Fluorescent particles are detected upon diffusion through
859 the confocal volume. (**B**) Autocorrelation data obtained from unbound Cy5-labelled GP^{CL}. The
860 autocorrelation of individual 5-sec fluorescence intensity traces, normalized to the point at 10^{-2} ms, was
861 calculated (grey curves). The average of 100 autocorrelation curves (blue) was fitted to a model for a
862 single fluorescent species diffusing in 3 dimensions with photophysical (triplet state) dynamics (red; see
863 Materials and Methods). This analysis indicated that GP^{CL} has a diffusion time of $\tau_{protein}$ = 0.308 ± 0.007
864 ms. Photophysical dynamics were observed below 10^{-2} ms. (**C**) Autocorrelation curves comparing diffusion
865 times of GP^{CL} (blue; determined in (B)) and liposomes (yellow; determined in the same manner). The

866 diffusion time of liposomes is $\tau_{liposome}$ = 2.6 ± 0.2 ms, which is 8-fold longer than GP^{CL}, allowing for
867 identification of membrane-bound and unbound GP^{CL} in solution. (**D**) The percentage of GP^{CL} bound to
868 unlabelled liposomes determined by fitting autocorrelation data to a model for two fluorescent species
869 diffusing in 3 dimensions, liposome-bound and unbound GP^{CL} with diffusion times of 2.6 ms and 0.3 ms,
870 respectively (Materials and Methods). GP^{CL} binding to liposomes of varying lipid compositions was
871 measured at pH 5.5 as a function of Ca^{2+} concentration: PC:Ch (black circles), PC:PS:Ch (grey circles) and
872 PC:PS:BMP:Ch (orange circles). (**E**) Percentage of total GP^{CL} bound to PC:PS:BMP:Ch liposomes under the
873 indicated conditions. To ensure sensitivity to changes in the percentage of membrane binding of GP^{CL}
874 variants, a total lipid concentration of 0.5 mM was used such that a maximum of 50% wild-type GP^{CL} bound
875 to liposomes at low pH in the presence of Ca^{2+}. Indicated *p*-values were determined by *t*-test (ns, $p > 0.05$).
876 (**F**) Percentage of GP^{CL} bound to liposomes with varying PS concentration and fixed BMP and Ch. GPCL-
877 liposome binding was evaluated in the absence (grey; 1 mM EDTA) or presence of 1 mM Ca^{2+} (orange). (**G**)
878 The ratio of bound GP^{CL} in the presence of Ca^{2+}, to bound GP^{CL} in the absence of Ca^{2+} for liposomes of
879 varying PS concentration (as in (F)). Data were fitted to a line with slope 0.003 (red line) with a 95%
880 confidence interval of -0.002 to 0.008 (black dashed lines), which was not significantly different from zero
881 ($p = 0.12$). (D-G) Data points or bars are presented as the mean ± standard error determined from three
882 sets of measurements.

883

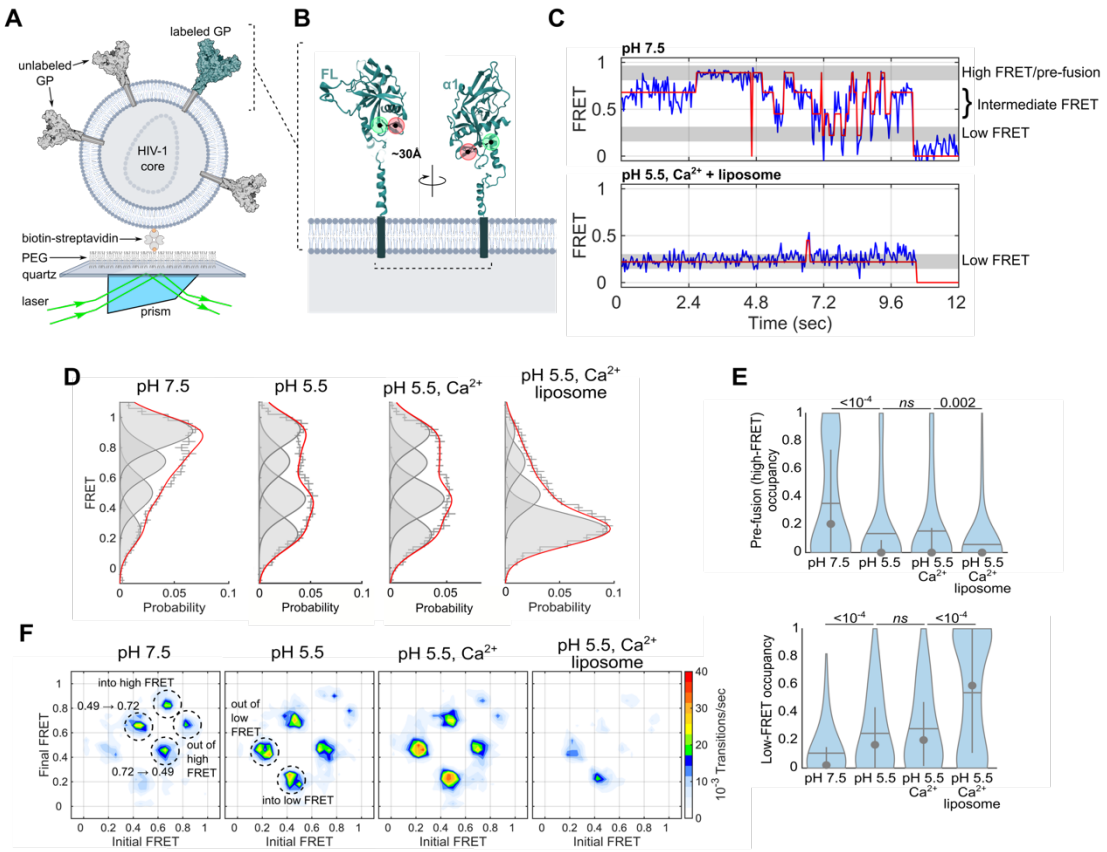

Figure 2. Acidic pH, Ca^{2+} and target membrane control GP conformational dynamics. (**A**) Experimental setup for smFRET imaging of pseudovirions labelled with Cy3 and Cy5 fluorophores. Labelled pseudovirions were immobilized on a passivated quartz microscope slide via a biotin-streptavidin linkage and imaged using prism-based TIRF microscopy. (**B**) Fluorophore attachment positions (red and green circles; residues 501 and 610 in GP2) are indicated on a GP protomer (PDB: 5JQ3). The indicated distance of 30 Å was previously determined through MD simulation of the fluorophore-labelled trimer [12]. (**C**) Representative FRET trajectories (blue) of GP^{CL} overlaid with idealization (red) determined through HMM analysis. The trajectory acquired at pH 7.5 (top) shows transitions between the pre-fusion conformation (0.92 ± 0.08 FRET), two intermediate-FRET states (0.72 ± 0.08 and 0.49 ± 0.08), and a low-FRET state (0.24 ± 0.08). In contrast, the FRET trajectory acquired in the presence of liposomes at pH 5.5 and 1 mM Ca^{2+} shows predominantly low FRET indicating a conformation stabilized by the presence of a target

896 membrane. (**D**) Histograms of experimentally observed FRET values for wild-type GP^{CL} under the
897 conditions indicated. Error bars indicate the mean probability per bin determined from three independent
898 groups of traces. Overlaid on the histograms are single Gaussian distributions (grey, shaded) indicating
899 the FRET states observed, which were generated during HMM analysis of the individual FRET trajectories.
900 The sum of the four Gaussian distributions is also overlaid in red. The zero-FRET state, which arises due to
901 photobleaching of the fluorophores is omitted to enable accurate visualization of the low-FRET state
902 occupancy. (**E**) Violin plots indicating the distribution of occupancy in the high-FRET pre-fusion (top) and
903 low-FRET (bottom) states. Overlaid on each plot is the median (circle), mean (horizontal line), and 25th and
904 75th quantile (vertical lines). Indicated *p*-values were determined by one-way ANOVA (ns, not significant).
905 (**F**) TDPs displaying the relative frequency of transitions of GP^{CL} under the conditions indicated. Specific
906 transitions between the observed FRET states are labelled with dashed circles.

907

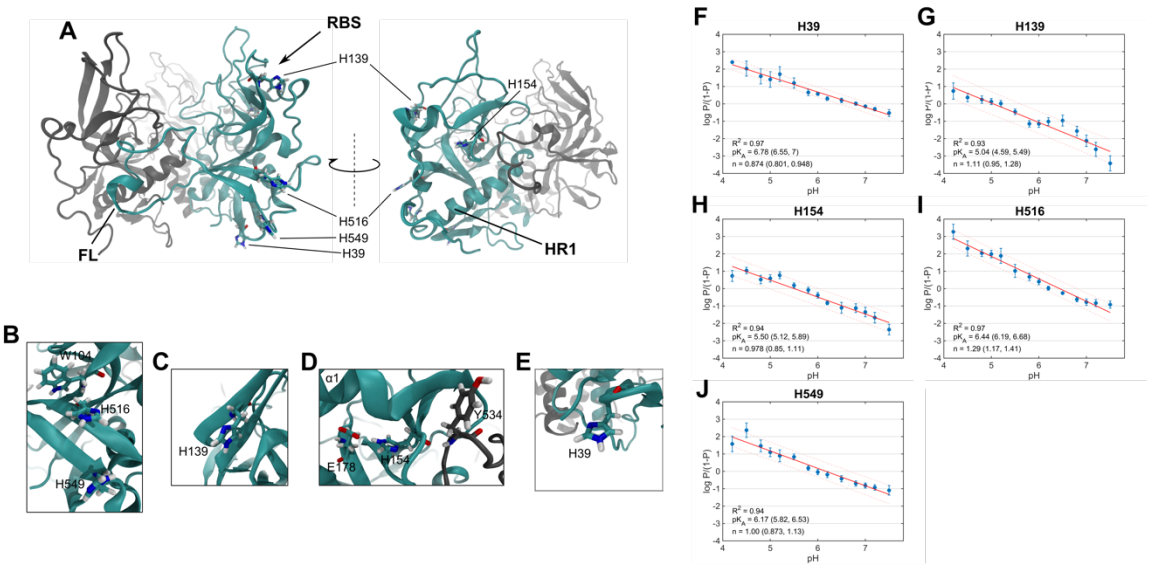

908

909 **Figure 3. Constant-pH MD simulations predict pK_a values of histidines in GP^{CL}.** (**A**) Cartoon rendering of
910 the trimeric GP^{CL} ectodomain (PDB: 5HJ3). One protomer within the trimer is highlighted in cyan. Also
911 indicated are structural landmarks (FL, fusion loop; RBS, receptor-binding site; HR1, heptad repeat 1) and
912 the 5 histidine residues that were considered in constant-pH MD simulations. (**B-E**) Zoomed-in views of
913 the 5 histidines and their surrounding residues. (**F**) Hill plot for H39 generated from the simulated titration
914 of the pH from 4.2 to 7.8. The fractional protonation (P) at each pH point is presented as the average ±
915 standard error determined from three simulation runs. The data were fitted to a linear model, resulting
916 in estimation of the pK_a and Hill coefficient (n), which are presented with 95% confidence intervals in
917 parentheses. The fit line is shown in red with 95% confidence intervals (dashed lines). Hill plots and fits
918 for (**G**) H139, (**H**) H154, (**I**) H516, and (**J**) H549 are displayed as in (F).

919

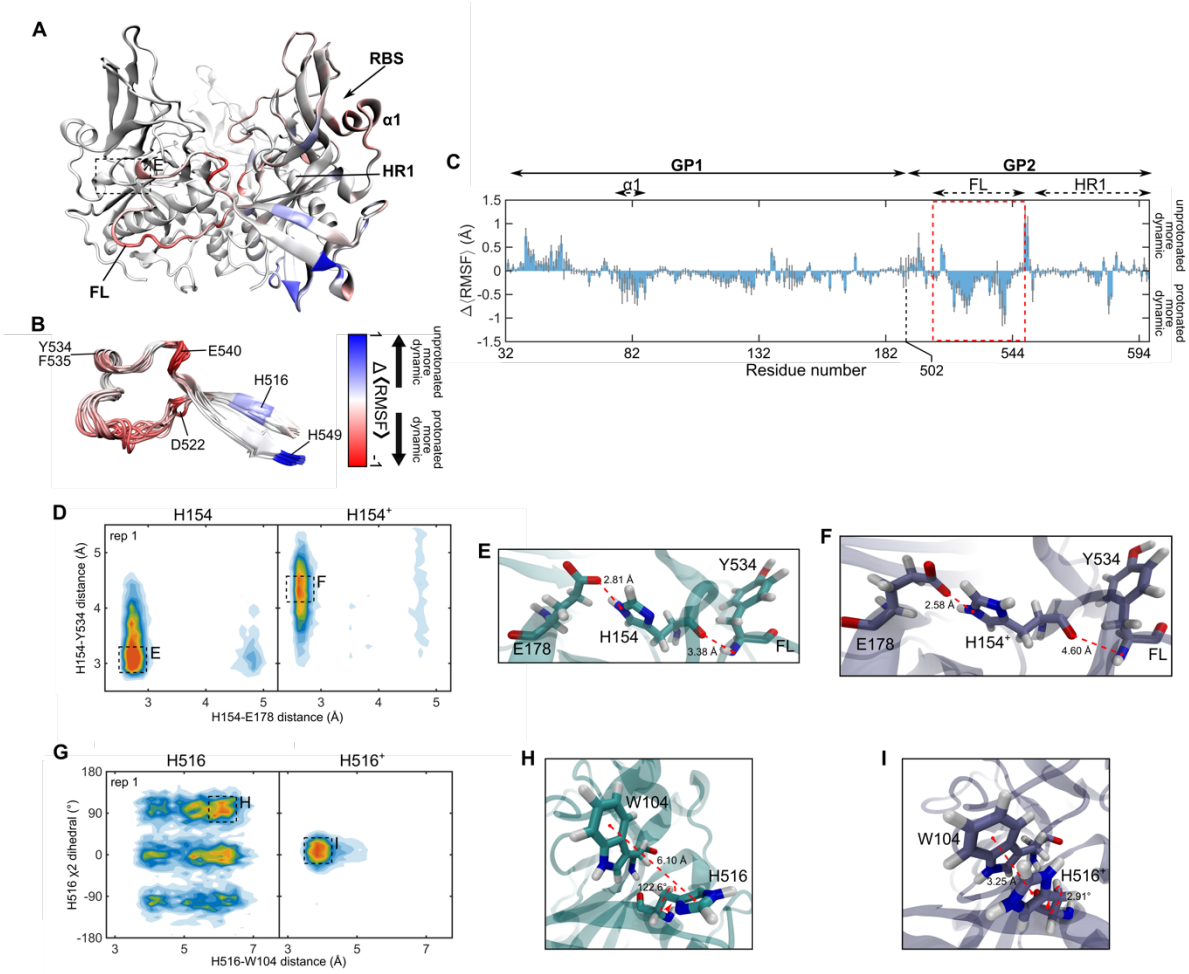

920

921 **Figure 4. MD simulations predict interactions that mediate GP^{CL} fusion loop stability.** (**A**) Cartoon
922 rendering of the trimeric GP^{CL} ectodomain (PDB: 5HJ3). One protomer within the trimer is highlighted with
923 a colored representation of the ΔRMSF. Red indicated regions that are more dynamic in the protonated
924 simulation; blue indicates more dynamics in the deprotonated simulation. Also indicated are structural
925 landmarks (FL, fusion loop; RBS, receptor-binding site; HR1, heptad repeat 1; α1 helix). (**B**) Overlay of nine
926 fusion loops from the three simulations of GP^{CL} trimers colored according to the ΔRMSF. Key residues,
927 which are discussed in the text, are highlighted. (**C**) ΔRMSF calculated from the simulations of GP^{CL} with
928 protonated and deprotonated histidines. The ΔRMSF for the fusion (FL) is highlighted with a red dashed
929 box. Data are presented as the mean ± standard error determined from the three replicate simulations.

930 (**D**) Contour plot indicating the position of H154 in terms of the distance between the H154 and E178
931 sidechains, and between the H154 and Y534 backbones. Data are shown for one of the three replicas of
932 the protonated ($H154^+$) and deprotonated (H154) simulations; data for the other two replicas are shown
933 in **Figure S1**. Predominant configurations are highlighted with dashed boxes and labelled with E and F. (**E**)
934 Zoomed-in view of a simulation frame depicting the interactions between H154, E178, and Y534 in the
935 configuration highlighted in (D), which predominated in the deprotonated simulation. (**F**) Corresponding
936 zoomed-in view of the configuration highlighted in (D), which predominated in the protonated simulation.
937 (**G**) Contour plot indicating the orientation of H516 in terms of the χ_2 sidechain dihedral and the distance
938 between the H516 and W104 side chains. Predominant conformations are highlighted with dashed boxes.
939 Data for the other two replicas are shown in **Figure S1**. (**H**) Zoomed-in view of a simulation frame depicting
940 the interactions between H516 and W104 in the configuration highlighted in (G), which predominated in
941 the deprotonated simulation. (**I**) Corresponding zoomed-in view of the configuration highlighted in (G),
942 which predominated in the protonated simulation.

943

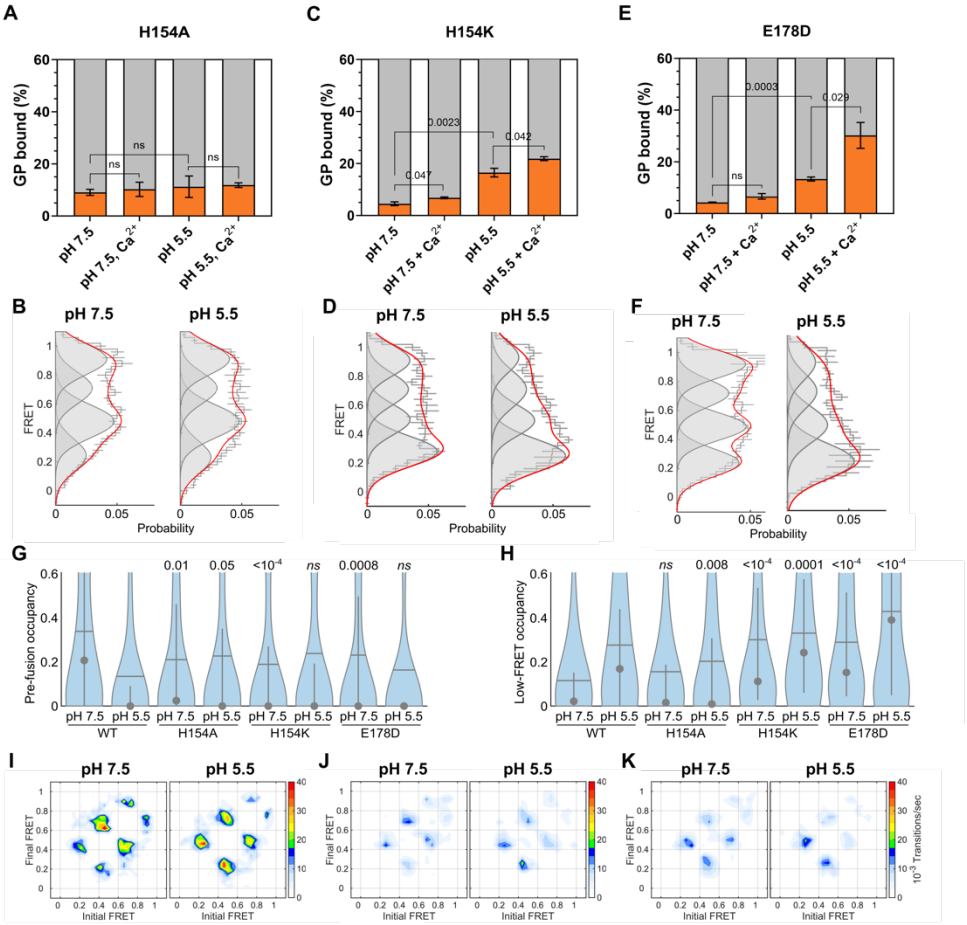

Figure 5. The H154-E178 interaction controls release of the fusion peptide to enable membrane binding. (**A**) Percentage of total GP^{CL} containing the H154A mutation bound to PC:PS:BMP:Ch liposomes under the indicated conditions determined by FCS. Indicated *p*-values were determined by *t*-test (ns, $p > 0.05$). (**B**) FRET histograms, displayed as in **Figure 2D**, for the H154A mutant at the indicated pH. (**C**) FCS and (**D**) smFRET data for the H154K mutant, indicating GP^{CL} membrane binding and conformation, respectively. (**E**) FCS and (**F**) smFRET data for the E178D mutant, indicating GP^{CL} membrane binding and conformation, respectively. (**G**) Violin plots indicating the distribution in high-FRET pre-fusion state occupancy and (**H**)

953 low-FRET state occupancy, displayed as in **Figure 2E**. (**I**) TDPs indicating the frequency of FRET transitions

954 at the indicated pH for the H154A mutant, the (**J**) H154K mutant, and the (**K**) E178D mutant.

955

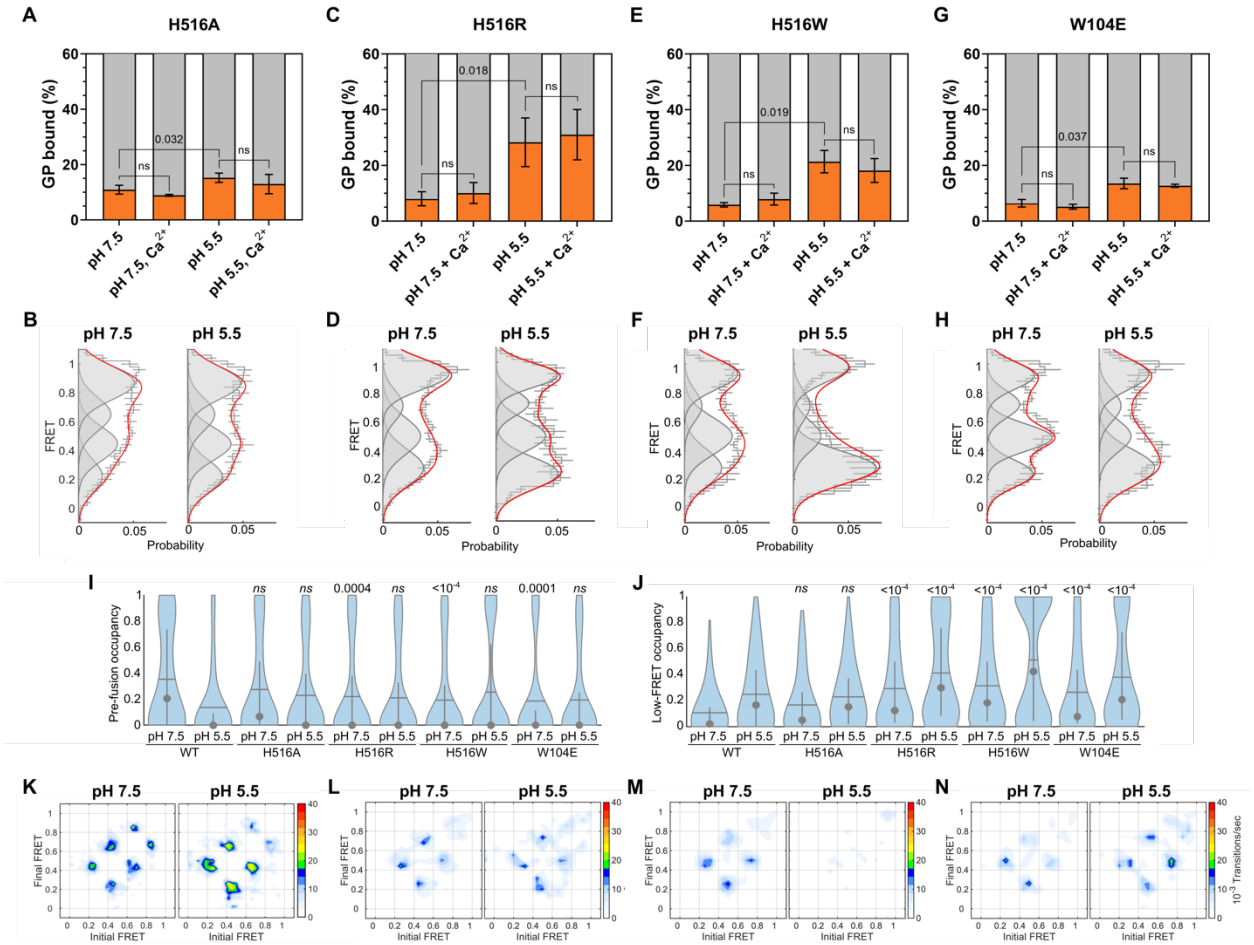

Figure 6. The H516-W104 interaction stabilizes the fusion peptide position for membrane binding. (**A**) Percentage of total GP^{CL} containing the H516A mutation bound to PC:PS:BMP:Ch liposomes under the indicated conditions determined by FCS. Indicated *p*-values were determined by *t*-test (ns, $p > 0.05$). (**B**) FRET histograms, displayed as in **Figure 2D**, for the H516A mutant at the indicated pH. (**C**) FCS and (**D**) smFRET data for the H516R mutant, indicating GP^{CL} membrane binding and conformation, respectively. (**E**) FCS and (**F**) smFRET data for the H516W mutant, indicating GP^{CL} membrane binding and conformation, respectively. (**G**) FCS and (**H**) smFRET data for the W104E mutant, indicating GP^{CL} membrane binding and conformation, respectively. (**I**) Violin plots indicating the distribution in high-FRET pre-fusion state occupancy and (**J**) low-FRET state occupancy, displayed as in **Figure 2E**. (**K**) TDPs indicating the frequency

966 of FRET transitions at the indicated pH for the H516A mutant, the (**L**) H516R mutant, the (**M**) H516W

967 mutant, and the (**N**) W104E mutant.

968

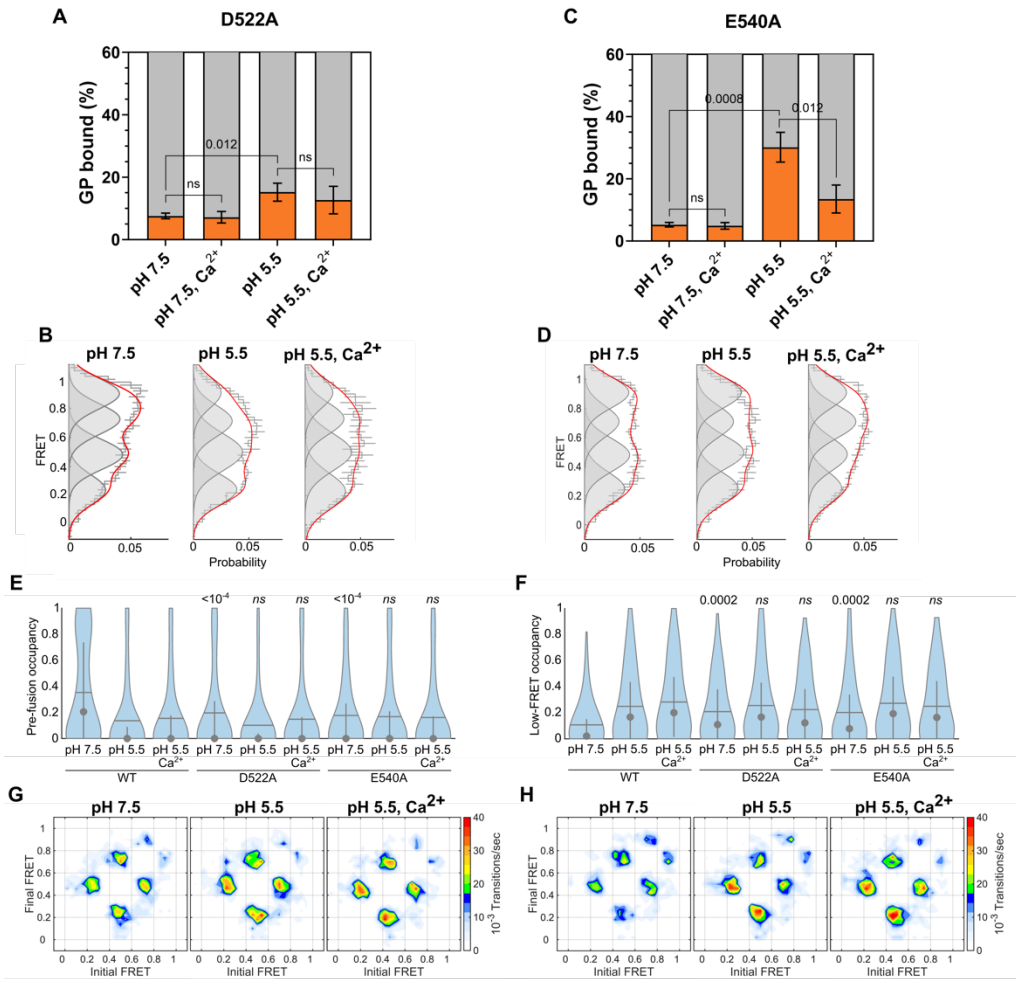

969

970 **Figure 7. D522 and E540 control Ca^{2+}-mediated GP^{CL} membrane binding.** (**A**) Percentage of total GP^{CL}
971 containing the D522A mutation bound to PC:PS:BMP:Ch liposomes under the indicated conditions
972 determined by FCS. Indicated *p*-values were determined by *t*-test (ns, $p > 0.05$). (**B**) FRET histograms,
973 displayed as in **Figure 2D**, for the D522A mutant at the indicated conditions. (**C**) FCS and (**D**) smFRET data
974 for the E540A mutant, indicating GP^{CL} membrane binding and conformation, respectively. (**E**) Violin plots
975 indicating the distribution in high-FRET pre-fusion state occupancy and (**F**) low-FRET state occupancy,
976 displayed as in **Figure 2E**. (**G**) TDPs indicating the frequency of FRET transitions at the indicated conditions
977 for the D522A mutant, and the (**H**) E540A mutant.

978

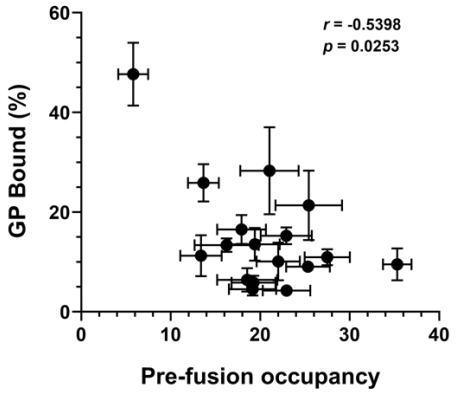

979

980 **Figure 8. GP^{CL} occupancy in the pre-fusion high-FRET conformation is inversely correlated with the**
981 **extent of membrane binding.** High-FRET pre-fusion state occupancy was determined through HMM
982 analysis of smFRET trajectories. Membrane binding was determined by FCS. The Pearson's correlation
983 coefficient (*r*) and associated *p*-value are indicated. Data for D522A and E540A (grey points) does not
984 correlate with membrane binding and were excluded from the analysis.

985

986 **Supporting Information Captions**

987 **Figure S1. Replicate data from MD simulation.** (**A**) Zoomed-in view of (purple) protonated and (cyan)
988 deprotonated simulation frames depicting an overlay of the interactions between H154, E178, and Y534.
989 (**B**) As in **Figure 4D**, contour plot indicates the position of H154 in terms of the distance between the H154
990 and E178 sidechains, and between the H154 and Y534 backbones. Data are shown for replicas two and
991 three of the protonated ($H154^+$) and deprotonated (H154) simulations. (**C**) Zoomed-in view of (purple)
992 protonated and (cyan) deprotonated simulation frames depicting an overlay of the interactions between
993 H516 and W104. (**D**) As in **Figure 4G**, contour plot indicating the orientation of H516 in terms of the χ_2
994 sidechain dihedral and the distance between the H516 and W104 side chains. Data are shown for replicas
995 two and three of the protonated ($H154^+$) and deprotonated (H154) simulations.

996 **Figure S2. Proteolysis, labelling, and infectivity of GP variants.** (**A**) Denaturing polyacrylamide gel showing
997 uncleaved GPΔTM and GP^{CL} (cleaved with HRV3C) imaged under Cy5 fluorescence (top) and stained with
998 Coomassie (bottom). (**B**) Comparison of relative infectivity of GPΔmuc, and GPΔmuc with the HRV3C
999 cleavage site. (**C**) (top) Western blot of pseudovirions showing expression of GPΔmuc (with the HRV3C
1000 cleavage site) and p24. (bottom) Relative infectivity of lentiviral pseudoparticles containing the mutant
1001 GPΔmuc. All infectivity experiments were performed with three biological replicates, each measured in
1002 triplicate. Data points represent the mean infectivity determined across biological replicates.

1003 **Figure S3. Antigenicity of mutant GPs.** (**A**) ELISA of wild-type and mutant GPΔTM proteins with mAb KZ52.
1004 Except for H154K, introduction of mutations in GPΔTM does not have a significant impact on the
1005 antigenicity of GP. ELISAs were carried out in triplicate. Data points represent absorbance values at 450
1006 nm. Bars and error bars represent the mean and standard deviations.

1007 **Figure S4. Model selection through minimization of the AIC and BIC.** smFRET trajectories from wild-type
1008 GP^{CL} were fit to a series of different models by maximum likelihood optimization using the MPL algorithm
1009 (see Materials and Methods). The maximized likelihood estimated for each model was corrected for
1010 differing numbers of model parameters using the AIC and BIC criteria. Under this procedure, the model
1011 with best fitness among those considered will generate minimum AIC and BIC values. Both criteria
1012 identified the 5-state linear model as providing the best representation of the data among the models
1013 considered. Overlaid on the plot are schematic representations of the kinetics models considered. In all
1014 models, the 0 state corresponds to the 0-FRET state, with the others reflecting non-zero FRET states. Lines
1015 represent connections (allowed transitions) between states. All non-zero FRET states are connected to
1016 the 0-FRET state since photobleaching is seen from all FRET states. TDPs shown in **Figures 2** and **5-7**
1017 support the identification of a linear model.